

Henrique Manuel Alferes Simões Vieira da Mota

# Modelling the hyper-viscoelastic behaviour of synthetic rubbers applied to rubber pad forming

Submitted in Partial Fulfilment of the Requirements for the Degree of Master in  
Mechanical Engineering in the speciality of Production and Project

Coimbra, July, 2018







UNIVERSIDADE D  
COIMBRA

FACULDADE  
DE CIÊNCIAS  
E TECNOLOGIA

# **Modelling the hyper-viscoelastic behaviour of synthetic rubbers applied to rubber pad forming**

Submitted in Partial Fulfilment of the Requirements for the Degree of Master in Mechanical Engineering in the speciality of Production and Project

## **Modelação do comportamento hiper-viscoelástico de borrachas sintéticas aplicado ao processo de conformação com borracha.**

Author

**Henrique Manuel Alferes Simões Vieira da Mota**

Advisor

**Diogo Mariano Simões Neto**

Jury

President	Professor Doutor Amílcar Lopes Ramalho Professor Associado da Universidade de Coimbra
Vowel	Professor Doutor José Luís Carvalho Martins Alves Professor Associado da Universidade do Minho
Advisor	Professor Doutor Diogo Mariano Simões Neto Professor Auxiliar Convidado da Universidade de Coimbra

**Coimbra, July, 2018**



*You must be imaginative, strong-hearted. You must try things that may not work, and you must not let anyone define your limits because of where you come from. Your only limit is your soul. What I say is true - anyone can cook... but only the fearless can be great.*

Gusteau in Ratatouille



## ACKNOWLEDGEMENTS

First, I wish to express my gratitude to my advisor, Professor Diogo Neto, for the constructive guidance, motivation and total availability to answer all my questions. I could not have asked for a better advisor – your spirit made me push myself to the next level and believe in the work we were doing.

To the fellow laboratory co-workers, I would like to take this paragraph to thank them for their advice and friendship. They surely contributed to a more relaxed work environment. On a special note, I would like to acknowledge João Barros and Bruno Martins for helping in the production of the Abaqus model.

To Professor Marta Oliveira, Professor José Luís Alves and Professor Amílcar Ramalho, I would like to express my sincere gratitude for your willingness to share some of your time and knowledge with me, throughout our scientific meetings.

Furthermore, this dissertation would not be possible without the help and support of my family, friends and Mafalda. Lastly, this is dedicated to my parents, for all the encouragement, sacrifice and unconditional support. Thank you for making me enjoy learning new things and take new heights in life, making me be who I am today.

This work was carried out under the project “Improving the manufacturing of metallic bipolar plates for fuel cells using the rubber forming process” with reference P2020-PTDC/EMS-TEC/0702/2014 (POCI-01-0145-FEDER-016779) funded by the Foundation for Science and Technology and the EU/FEDER, through the program COMPETE 2020. The support under the project MATIS (CENTRO-01-0145-FEDER-000014) is also acknowledged.







## Abstract

Fuel cells are a promising alternative to the combustion engines in the automotive industry, allowing to reduce significantly the air pollution generated by cars. However, this new technology still presents some economic issues due to the cost involved in the production of the bipolar plates (main component of fuel cells). In order to reduce the production costs, the rubber pad forming has been adopted in the manufacturing of thin stamped bipolar plates. Since the plastic deformation of the sheet is induced by a pad of rubber like material, the numerical modelling of this manufacturing process requires a deep knowledge about the mechanical behaviour of rubber materials.

The main objective of this study is the numerical modelling of rubber-like materials, which typically present a hyper-viscoelastic behaviour. Accordingly, the constitutive law currently implemented in the V-Biomech finite element code, used to describe the mechanical behaviour of rubbers, is presented in detail. Hence, the hyperelastic behaviour is described by the Mooney-Rivlin model, while the viscoelasticity is modelled by a series of Maxwell elements. Considering the case of uniaxial compression stress state, the closed-form solution is derived for the hyper-viscoelastic behaviour, which is posteriorly used in the procedure to identify the material parameters involved in the constitutive model. Two different polyurethane materials are experimentally evaluated by means of uniaxial compression tests and relaxation tests, allowing to identify the material parameters by fitting the numerical model to the experimental data. Then, these rubber materials are adopted in the numerical simulation of the rubber pad forming process, using the Abaqus software to study numerically the forming of metallic bipolar plates.

Taking into account the experimental results from both the uniaxial compression tests and relaxations tests performed on two different polyurethanes, the viscosity effect is small considering the range of velocity applied, particularly for the rubber with lower hardness value. Moreover, the predicted mechanical behaviour of both rubbers is in good agreement with the experimental values. The numerical results of the rubber pad forming process show that the final thickness of the stamped bipolar plate is not significantly influenced by the rubber hardness. However, the predicted final thickness distribution is more uniform in comparison with the one obtained with the conventional stamping process.

The maximum value of thinning occurs always in the fillet radius of the rib, which is the zone with large plastic deformation.

**Keywords** Metallic bipolar plates, Rubber pad forming, Numerical simulation, Synthetic rubber, Hyper-viscoelastic behaviour.

## Resumo

As células de combustível são atualmente uma alternativa viável ao uso de motores de combustão interna na indústria automóvel, permitindo uma redução significativa da poluição atmosférica gerada pelos automóveis. Ainda assim, esta tecnologia apresenta alguns problemas económicos devido ao custo de produção das placas bipolares (componente principal das células de combustível). De modo a reduzir o custo de produção, a conformação por borracha é adotada na produção das placas bipolares. Atendendo a que a deformação plástica da placa bipolar é conseguida através de um punção de borracha, a modelação numérica do processo requer um conhecimento profundo acerca do comportamento mecânico de borrachas.

O principal objetivo deste estudo consiste na modelação da borracha, que tipicamente apresenta um comportamento hiper-viscoelástico. Assim, o modelo constitutivo implementado no software V-Biomech é apresentado em detalhe. Consequentemente, o comportamento hiperelástico é descrito pelo modelo constitutivo Mooney-Rivlin, enquanto que a viscoelasticidade é caracterizada por uma série de elementos de Maxwell. Considerando o estado de tensão de compressão uniaxial, a solução explícita é obtida para o comportamento hiper-viscoelástico, e posteriormente usada na identificação dos parâmetros do material. Dois provetes de poliuretano são avaliados experimentalmente através de ensaios de compressão uniaxial e de ensaios de relaxação, permitindo a identificação dos parâmetros do material através de uma aproximação entre os dados experimentais e o modelo numérico. Posteriormente, os referidos materiais são utilizados na simulação numérica do processo de conformação por borracha, utilizando o software Abaqus para estudar numericamente a conformação das placas bipolares metálicas.

Considerando os dados experimentais obtidos através dos ensaios de compressão e de relaxação, efetuados nos dois provetes de poliuretano, o efeito da viscosidade é pequeno, considerando a gama de velocidade aplicada, particularmente para o provete com menor dureza. Adicionalmente, o comportamento mecânico obtido para os dois materiais está em conformidade com os resultados experimentais. Os resultados numéricos do processo de conformação por borracha mostram que a espessura final da placa bipolar não é significativamente afetada pela dureza da borracha. Ainda assim, a espessura final prevista

é mais uniforme em comparação com o processo de estampagem clássico. O valor máximo de redução de espessura ocorre sempre na curvatura superior da placa.

**Palavras-chave:** Placa bipolar metálica, Conformação com borracha, Simulação numérica, Borracha sintética, Comportamento hiper-viscoelástico.

## Contents

LIST OF FIGURES .....	ix
LIST OF TABLES .....	xi
SIMBOLOGY AND ACRONYMS .....	xiii
Roman symbols .....	xiii
Greek symbols .....	xv
Acronyms .....	xvi
1. INTRODUCTION .....	1
1.1. Historical review of the rubber .....	3
1.2. Rubber characterization .....	4
1.3. V-Biomech FEM code .....	4
1.4. Objectives and dissertation outline .....	5
2. BACKGROUND THEORY .....	7
2.1. Finite element method .....	7
2.2. Mixed u/P formulation .....	7
2.3. Finite strain theory .....	8
3. CONSTITUTIVE MODEL FOR RUBBER LIKE MATERIALS .....	11
3.1. Hyperelasticity .....	11
3.1.1. Strain Energy Function .....	12
3.1.2. Mooney-Rivlin constitutive model .....	12
3.1.3. Stress evaluation: second Piola-Kirchhoff .....	14
3.1.4. Uniaxial stress state under incompressible conditions .....	15
3.2. Viscoelasticity .....	18
3.3. Hyper-viscoelasticity .....	20
3.3.1. Viscoelasticity modes in V-Biomech .....	20
3.3.2. Mode I: uniaxial compression .....	22
3.3.3. Mode III: uniaxial compression .....	26
4. FINITE ELEMENT SOLUTION .....	27
4.1. Case study: uniaxial stress .....	27
4.2. Nearly incompressible behaviour .....	30
4.3. Strain rate effect in viscoelasticity .....	32
4.4. Viscoelasticity modes in V-Biomech .....	34
4.5. Hyper-viscoelastic behaviour .....	36
4.6. Comparison between V-Biomech and Abaqus .....	37
5. EXPERIMENTAL TESTS .....	39
5.1. Experimental procedure and results .....	39
5.2. Material parameters identification – curve fitting .....	44
5.3. Numerical model accuracy .....	46
6. RUBBER PAD FORMING SIMULATION .....	51
6.1. Finite element model .....	52
6.2. Results and discussion .....	55

7. CONCLUSIONS .....	61
BIBLIOGRAPHY .....	63

## LIST OF FIGURES

Figure 1.1. Proton exchange membrane fuel cells basic setup including the bipolar plates with a serpentine flow field design.....	1
Figure 1.2. Rubber pad forming scheme including the rigid die, sheet metal and rubber pad. ....	3
Figure 2.1. Stress decomposition scheme into hydrostatic and deviatoric contributions.....	8
Figure 2.2. Decomposition of deformation gradient tensor into volumetric and deviatoric components.....	9
Figure 3.1. Comparison between linear and non-linear stress – strain curves in elastic domain. ....	11
Figure 3.2. Comparison between experimental and numerical results of stress-stretch curves under uniaxial tension conditions for silicone-rubber material [12].....	13
Figure 3.3. Initial and final configuration of a cube under uniaxial traction along $x_1$ direction.....	15
Figure 3.4. Rheological analogy approach representing the generalized Maxwell model..	19
Figure 3.5. Scheme drawing of the 2 V-Biomech modes that sums the mechanical behaviour of each one.....	21
Figure 4.1. Discretization of the cube adopted in the numerical simulation of the uniaxial compression test and z displacement distribution after loading. ....	28
Figure 4.2. Contribution of each component composing the second Piola Kirchhoff stress in the uniaxial compression test. ....	30
Figure 4.3. Comparison between incompressible material (analytical) and nearly incompressible (V-Biomech simulation) in the uniaxial compression test assuming only hyperelastic behaviour (Mooney-Rivlin). ....	32
Figure 4.4. Influence of the prescribed displacement velocity on the predicted second Piola Kirchhoff stress considering the uniaxial compression test. ....	33
Figure 4.5. Deviatoric and volumetric stress components considering the mode I and mode III of viscoelasticity in the uniaxial compression test. ....	35
Figure 4.6. Comparison between different predictions for the hydrostatic stress component in the uniaxial compression test considering the mode I of the viscoelasticity. ...	36
Figure 4.7. Comparison of the second Piola Kirchhoff stress obtained by numerical simulation (V-Biomech) and predicted with equation (3.61), in case of mode I and equation (3.62) in case of mode III. ....	37
Figure 4.8. Comparison between the second Piola Kirchhoff stress predicted by Abaqus and V-Biomech (mode I and mode III) finite element codes in the uniaxial compression test. ....	38

Figure 5.1. Test specimens after being properly cut to their desired shape and ready to use in the experimental tests.....	39
Figure 5.2. Shimadzu tensile testing machine setup, combined with the yellow and orange PUR, and the improvised compression plates.....	41
Figure 5.3. Experimental setup including: (a) the tests specimen, the lubrication used, the improvised compression plates and (b) the tensile testing machine. ....	42
Figure 5.4. Experimental evolution of the second Piola Kirchhoff stress obtained from the yellow PUR experimental tests: (a) uniaxial compression tests at different values of grip velocity and (b) relaxation test. ....	43
Figure 5.5. Experimental evolution of the second Piola Kirchhoff stress obtained from the orange PUR experimental tests: (a) uniaxial compression tests at different values of grip velocity and (b) relaxation test. ....	44
Figure 5.6. Comparison between the experimental solution and the first and forth combination methods: (a) second Piola-Kirchhoff stress and (b) relative error. ...	46
Figure 5.7. Stress-stretch comparison between the experimental results and the different solutions obtained for each material and viscoelasticity mode, while considering the slowest grip velocity of the compression tests. ....	47
Figure 5.8. Stress-stretch comparison between the experimental results and the different solutions obtained for each material and viscoelasticity mode, while considering the relaxation tests.....	49
Figure 6.1. Rubber pad forming process assembly scheme: (a) original straight channel forming process and (b) the one used for finite element analysis.....	51
Figure 6.2. Sheet metal geometry in the conventional stamping for several channels. ....	51
Figure 6.3. Example of a bipolar plate manufactured by forming. ....	52
Figure 6.4. Rubber pad geometry and mesh used in the finite element analysis. ....	54
Figure 6.5. Sheet metal geometry and mesh used in the finite element analysis. ....	54
Figure 6.6. Predicted von Mises stress distribution in the sheet and rubber at four different instants of the rubber pad forming considering the orange PUR in the rubber.....	56
Figure 6.7. Comparison of final thickness distribution as function of the initial x coordinate, considering two different rubbers in the rubber pad forming and the conventional stamping process. ....	57
Figure 6.8. Evolution of the maximum thinning and punch force for both rubber material in the rubber pad forming of a bipolar plate and comparison with the conventional stamping. ....	58
Figure 6.9. Predicted von Mises stress distribution in the rubber at the end of the forming process comparing two different materials for the rubber. ....	59
Figure 6.10. Equivalent plastic strain distribution on both rubber pad process simulation and the conventional stamping process.....	60



## LIST OF TABLES

Table 1.1. Advantages and disadvantages of the rubber pad forming process.....	2
Table 3.1. Component of the stress tensors in the loading direction considering the Mooney-Rivlin constitutive model with 2 parameters. ....	18
Table 3.2. Component of the second Piola Kirchhoff stress tensor in the loading direction considering the Mooney-Rivlin constitutive model with 2 and 5 parameters.....	18
Table 4.1. Parameters of the Mooney-Rivlin constitutive model (hyperelasticity) and for the two Maxwell elements (viscoelasticity). ....	27
Table 4.2. Time and displacement history considered in the uniaxial compression test.....	27
Table 4.3. Relationship between the ratio bulk /shear modulus and the Poisson ratio according to the V-Biomech finite element code. ....	31
Table 5.1. Dimensions (nominal and real) and hardness of both materials used in the experimental tests. ....	40
Table 5.2. Experimental tests summary including test specimen, type of test, loading velocity and time. ....	41
Table 5.3. Material parameters of the constitutive model (Mooney-Rivlin and Maxwell elements) identified for both materials and for both viscoelasticity modes.....	46
Table 5.4. Last increment analysis for the experimental tests and the four simulations at different grip velocities, including the different materials and viscoelasticity modes.....	48
Table 6.1. Reference values for the main dimensions of the desired product. ....	52
Table 6.2. Material parameters used in the isotropic Swift hardening law to describe the metallic material. ....	53
Table 6.3. Loading velocity, time history and rubber displacement for both rubber materials. ....	55



## SIMBOLOGY AND ACRONYMS

### Roman symbols

Relationship between spring stiffness	$ak_i$
Initial section area	$A_i$
Final section area	$A_f$
Mooney-Rivlin constitutive model parameters.	$C_{10}, C_{01}, C_{11}, C_{20}, C_{02}$
Coefficients used to predict hydrostatic stress component	$c_1, c_2$
Right Cauchy-Green strain tensor	$\mathbf{C}$
Deviatoric contribution of the right Cauchy-Green strain tensor	$\bar{\mathbf{C}}$
Abaqus compressibility parameter	$D$
Young's Modulus	$E$
Green-Lagrange strain tensor	$\mathbf{E}$
Deformation gradient tensor	$\mathbf{F}$
Deviatoric contribution of the deformation gradient tensor	$\bar{\mathbf{F}}$
Shear Modulus	$G$
Prony series parameter	$\bar{g}_l^p$
Prony series function	$g_R$
Viscoelastic stress contribution	$h_j$
Second order unit tensor	$\mathbf{I}$
Isotropy-related invariants of the Right Cauchy-Green Tensor	$I_1, I_2, I_3$

Isotropy-related invariants of the deviatoric contribution of the Right Cauchy-Green strain tensor	$\bar{I}_1, \bar{I}_2, \bar{I}_3$
Jacobian of the deformation gradient tensor	$J$
Bulk Modulus	$K$
Initial length	$l_i$
Final length	$l_f$
Logarithmic strain component	LE
Number of Maxwell elements	M
Number of Prony elements	N
Hydrostatic stress component	$p$
Hydrostatic hyperelastic stress component	$p_{HE}$
First Piola-Kirchhoff stress tensor	$\mathbf{P}$
Pressure computed from the displacement field	$\bar{p}$
Pressure interpolated from the pressure field	$\tilde{p}$
Strain energy function term, which is function of both displacements and the interpolated pressure	$Q^0(J)$
Deviatoric stress component	$\mathbf{s}$
Total system deviatoric stress component	$S_{total}$
Hyperelastic deviatoric stress component	$S_{HE}$
Time instant	$t$
Right stretch tensor	$\mathbf{U}$
Strain energy function	$W(\mathbf{C})$
Volumetric strain energy function	$\bar{W}_H(J)$

---

Total deviatoric strain energy function	$\bar{W}(\bar{\mathbf{C}})$
Total deviatoric strain energy function considering the Mooney-Rivlin constitutive model.	$\bar{W}_{MR}(\bar{\mathbf{C}})$
Position vector of a given material point on the current configuration	$\mathbf{x}$
Position vector of a given material point on the reference configuration	$\mathbf{X}$
Flow stress	$Y$
Main dimensions of metallic bipolar plate	$w_1, s, h, r, R$
Swift law material parameters	$K, \varepsilon_0, n$

### **Greek symbols**

Characteristic relaxation function related to the elastic part	$\hat{\gamma}(t)$
Time increment	$\Delta t$
Displacement	$\Delta l$
Equivalent plastic strain	$\bar{\varepsilon}^p$
Damper constant	$\eta$
Principal stretch	$\lambda_1, \lambda_2, \lambda_3$
Stretch	$\lambda$
Spring stiffness	$\mu$
Poisson ratio	$\nu$
Second Piola-Kirchhoff stress tensor	$\mathbf{\Pi}$
Total Second Piola-Kirchhoff stress	$\Pi_{total}$

Hyperelastic Second Piola-Kirchhoff stress	$\Pi_{HE}$
Maxwell element Second Piola-Kirchhoff stress	$\Pi_{MW}$
Cauchy stress tensor	$\sigma$
Total system stress	$\sigma_{total}$
Total deviatoric system stress	$\sigma_{HE}$
Hyperelastic stress contribution	$\sigma_0$
Relaxation time	$\tau$

### Acronyms

Polyurethane	PUR
Proton exchange membrane	PEM
Two dimensional	2D
Three dimensional	3D

# 1. INTRODUCTION

Nowadays, society deals with the most polluted air that has ever covered the earth, which translates in excessive harmful gases, particles and molecules for people, animals and earth itself. Since carbon monoxide gas from combustion engines is one of the main pollutants, society is paving the way for alternative solutions, such as electric engines and reduction of car weight to reduce fuel consumption.

Today, proton exchange membrane (PEM) fuel cells are gathering major interest around the world as being one of the potential new sources of energy because of their high efficiency, fast start-up, potential of energy conservation, safety and environmental protection [1]. The main drawbacks are the high manufacturing cost and low durability, which prevented their widespread commercialization. One of the key components of these proton exchange membrane fuel cells are the bipolar plates, which are responsible for supplying a uniform distribution of reactant gases over the electrodes via flow channels, among other responsibilities [2]. Thus, giving a lot of importance to the desired flow field design, since it deals directly with the performance of fuel cells. Among the classic flow field design solution, the serpentine flow field is the most commonly used design in the commercial fuel cells [3]. Figure 1.1 shows the insides of this kind of fuel cells with the presence of a serpentine flow field.

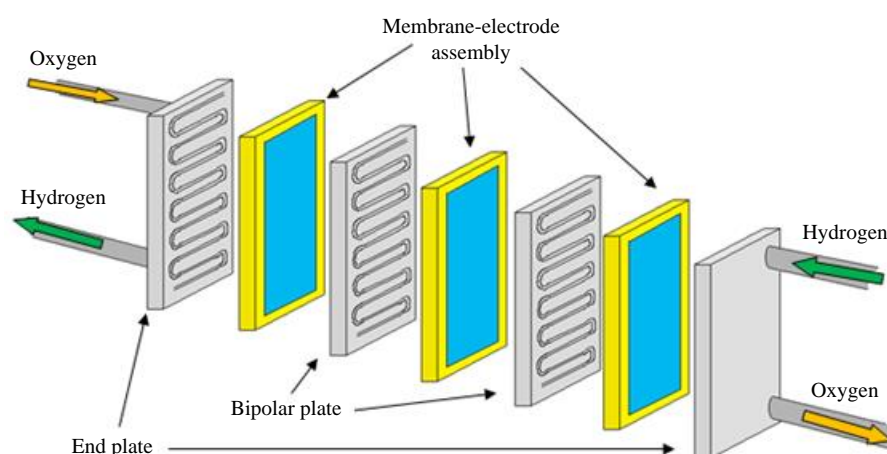


**Figure 1.1.** Proton exchange membrane fuel cells basic setup including the bipolar plates with a serpentine flow field design.

However, the current production cost of a fuel cell is 4-10 times higher than an internal combustion engine, with the bipolar plate representing 30-45% of the stack cost. Hence, the production of the bipolar plate is the largest bottleneck for its commercialization. From the three main types of bipolar plates (metallic, graphite and polymer-carbon composite), there is one with special interest due to its low cost, ease of production and excellent mechanical, electrical and thermal properties, which is the metallic bipolar plate. The high production rates associated with the stamping process make it adequate to manufacture metallic bipolar plates.

As an alternative to the classic stamping process, this study will address the rubber pad forming process, which uses a rubber pad inside a container (rigid). This new method uses only one rigid die, which is placed underneath the sheet metal, and one rubber pad, which is placed on top of the sheet metal (see Figure 1.2). Note that the relative positions can be interchanged. The main advantages and disadvantages of this method, over the classical sheet metal forming processes can be found in Table 1.1.

**Table 1.1.** Advantages and disadvantages of the rubber pad forming process.

Advantages	Disadvantages
<ul style="list-style-type: none"><li>• Fewer components and lower tool cost for small series</li></ul>	<ul style="list-style-type: none"><li>• Need for a higher capacity press machine</li></ul>
<ul style="list-style-type: none"><li>• The rubber pad can be used for several different shapes of die</li></ul>	<ul style="list-style-type: none"><li>• Rubber pad with limited lifetime</li></ul>
<ul style="list-style-type: none"><li>• More uniform thickness distribution</li></ul>	<ul style="list-style-type: none"><li>• Slow rate of production</li></ul>
<ul style="list-style-type: none"><li>• Shorter set-up time, as no lining-up of tools is necessary</li></ul>	<ul style="list-style-type: none"><li>• Restrict temperature range</li></ul>
<ul style="list-style-type: none"><li>• No marks on the metal surface in contact with the pad</li></ul>	
<ul style="list-style-type: none"><li>• No lubrication needed, usually</li></ul>	



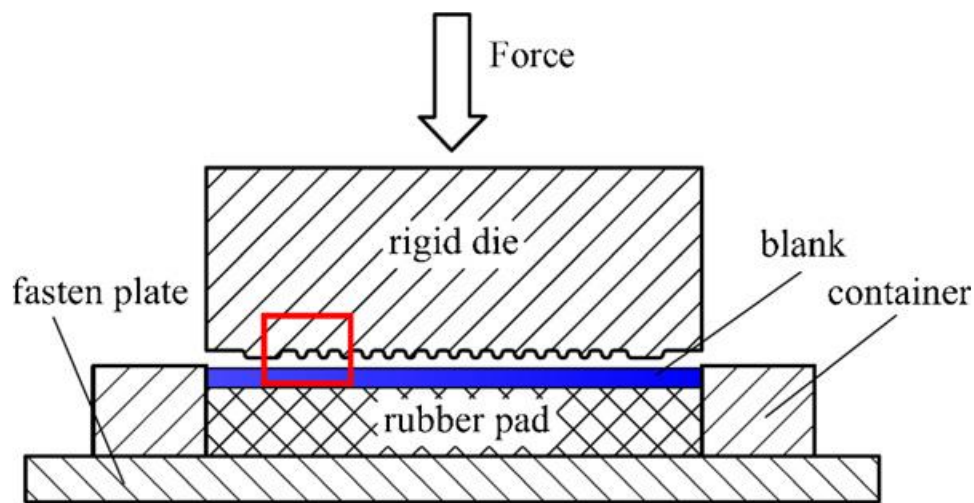


**Figure 1.2.** Rubber pad forming scheme including the rigid die, sheet metal and rubber pad.

### 1.1. Historical review of the rubber

Before the advent of synthetic polymers, natural rubber obtained from trees was the only source of rubber [4]. Originally discovered in South America, the first rubber balls were brought to Europe by Christopher Columbus after his second voyage to the West Indies. Later on, scientists began to investigate such material because of its elasticity and waterproofing, and thus marking the rubber industry in Europe in the late 1700s.

Whilst the rubber industry was quickly increasing in the soft weather of Europe, the US industry was dealing with its susceptibility to changes in temperature, representing difficulties for the early factories, since excessive temperatures made the products sticky. In 1839, this problem was brought to Charles Goodyear, an American inventor, who became the discoverer of rubber vulcanization, solving the presented challenge by heating rubber with sulphur.

From that time on, the natural rubber industry began to expand and was fuelled by additional supplies of rubber from the Far East. In 1888, John Boyd Dunlop re-invented the pneumatic tyre, thus giving birth to the future main consumer of natural rubber. The Second World War had a vast impact on rubber history. Since there was an interruption of natural rubber supply, developed countries took on the challenge of creating methods for bulk production, thus producing synthetic rubber. Nowadays, rubber materials are present in our daily life and can be found in the most common places, like automotive industry, footwear, foams, belting, seals, hoses, wires and so on.

## **1.2. Rubber characterization**

In the mid-1900s, physicians Melvin Mooney and Ronald Rivlin noticed that the relationship between stress and strain for rubber materials was non-linear, therefore contradicting the linear theory of elasticity, Hooke's law, used since the 17<sup>th</sup> century. These two scientists presented the first constitutive laws used to describe rubber materials, thus opening doors to many others who would contribute to this investigation, like Raymond Ogden in 1972.

From experimental observations, it has been shown that for nearly any material there is a certain amount of energy absorbing behaviour, thus contradicting purely elastic materials. A large class of dissipative materials are described by a time-dependent viscoelastic constitutive model, which have been studied since 1976 by Findley, Lai and Onaran [5]. These materials tend to show properties like relaxation, creep, time-dependent stiffness and strain-rate-dependent hysteretic behaviour.

Today, it is known that, in order to correctly describe rubber behaviour, there is a need for understanding two different concepts: hyperelasticity and viscoelasticity. The hyper-viscoelastic model combines both formulations, in which the viscoelasticity is also dependent on the hyperelasticity, thus implying that the deformation history is of great importance.

## **1.3. V-Biomech FEM code**

The adoption of open source finite element codes by the scientific community presents great advantages over the commercial finite element packages (e.g. Abaqus) because there is total access to source code. Accordingly, in the present study the in-house finite element software V-Biomech is adopted, which was developed by Alves et al [6] to simulate the hyper-viscoelastic behaviour of nearly incompressible materials (including soft tissues). This numerical tool allows the numerical simulation of soft tissues, isotropic and anisotropic hyperelasticity, muscle activation and short and long term viscous effects. It uses a total Lagrangian formulation and the solution approximation is obtained through a fully implicit time integration scheme. In order to characterize the behaviour of nearly incompressible soft tissues, it decomposes the deformation gradient into two parts: volumetric and deviatoric, assuming a u/P interpolation taking into account the displacement and pressure fields.

In this section there will be a brief introduction to the inputs and outputs of V-Biomech, to understand what can be changed and what can we expect to obtain. As input, the program needs to read four different text files:

1. BCID – contains information about the boundary conditions.
2. BIO – defines maximum number of steps, convergence criterion, maximum number of iterations, maximum time increment, and information related to time history of loading and muscle activation.
3. MSH – covers the spatial discretization (finite elements and nodes).
4. Mater1 – gives information about material properties such as: constitutive model, bulk modulus, muscle activation and membrane criteria and viscous parameters.

By definition, V-Biomech retrieves the following outputs:

1. GID files with stress and strain measurements.
2. Total force and displacement in surfaces with applied boundary conditions.
3. Volume history.

In order to obtain more output information, the user can use the input OUTdata.dat text file to requests for information about a given Gauss point, extracting extra stress tensors - second Piola-Kirchhoff and Cauchy; and Green-Lagrange deformation tensor.

## **1.4. Objectives and dissertation outline**

The main objective of this study is the numerical modelling of rubber-like materials, which typically present a hyper-viscoelastic behaviour. In the present study the hyperelastic behaviour is described by the Mooney-Rivlin constitutive model, while the viscoelasticity is modelled by Maxwell elements. Accordingly, the identification of the material parameters requires experimental data, which is obtained from uniaxial compression tests and relaxation tests of two different polyurethanes. Finally, the goal is the numerical study of the rubber pad forming process applied in the manufacture of metallic bipolar plates.

The present dissertation has seven different chapters: “Introduction”, “Background theory”, “Constitutive model for rubber like materials”, “Finite element solution”, “Experimental tests”, “Rubber pad forming simulation”, and “Conclusions”.

The present chapter, “Introduction”, provides a brief introduction about the innovative process of rubber pad forming applied in the manufacture of the metallic bipolar plates for fuel cells, which is the main focus of this work. The history of rubber industrialization, its characterization and the V-Biomech software, which will be used throughout this study, are presented.

The second chapter, “Background Theory”, aims to help the reader revive some notions about finite strain theory and the applied finite element method with u/P formulation. This will be of extreme usefulness, in order to understand the deductions and calculations made down the road.

The third chapter “Constitutive model for rubber like materials”, describes how rubber behaviour can be mathematically described by constitutive laws, defining the hyperelasticity and the viscoelasticity. Furthermore, closed-form solutions are proposed to evaluate the stress state for uniaxial compression assuming material incompressibility.

The fourth chapter “Finite element solution”, shows that the proposed closed-form solutions on the previous chapter match the solutions predicted by V-Biomech and Abaqus finite element codes, considering the uniaxial compression.

The fifth chapter “Experimental Tests”, presents the experimental procedure and results from the uniaxial compression tests and relaxation tests carried out on two different rubber materials. Then, using that experimental data, the material parameters involved in the constitutive model are obtained by curve fitting.

The sixth chapter, “Rubber Pad Forming”, contains the finite element analysis of the rubber pad forming process applied in the production of metallic bipolar plates, using the Abaqus software. The numerical model uses the mechanical behaviour of the rubbers analysed before, considering plane strain conditions to simplify the analysis. The final goal is to compare the two different rubber materials in the rubber pad forming, as well as compare this new process with the conventional one.

The last chapter, “Conclusions”, provides the conclusions from each chapter, not only describing the results acquired, but also highlighting some of the issue encountered. Finally, a brief summary of future works is included.

## 2. BACKGROUND THEORY

### 2.1. Finite element method

With its enormous importance to the engineering world, the finite element method has been object of study since the 1940s, marking the way engineers solve problems with the simple idea of dividing a complex system into a finite number of well-defined components. This leads to a discrete solution that represents an approximation, which hopefully approximates the real continuum solution as the number of discrete variables increases [7]. The finite element method can be found in an extensive variety of engineering applications such as project design, structural mechanics and even heat transfer and fluid flow. Time discretization becomes imperative in transient problems, like the ones addressed in this study (hyper-viscoelastic behaviour). Consequently, two different methods can be used to perform the time integration: implicit and explicit. The implicit method requires the solution of a system of non-linear equations in each increment, whereas the explicit method only solves a system of linear equations in each increment but requires much more increments to guarantee a stable and accurate solution.

### 2.2. Mixed u/P formulation

The standard displacement formulation can generate problems when the Poisson's ratio becomes higher than 0.4 (typical in rubbers). If the material behavior is considered incompressible or nearly incompressible, the Poisson ratio tends to 0.5 and the bulk modulus tends to infinity. This will lead to a volumetric strain tending to zero and generally results in null displacement solutions because displacement-based elements are not formulated to deal with this condition. This results in numerical difficulties and can exhibit overly stiff behavior caused by volumetric locking. The problem with using a standard displacement formulation lies with the calculation of the mean stress or pressure, which is related to the volumetric part of the strain, for isotropic materials. The principal stress can be divided into the hydrostatic stress (pressure), which accounts for volume changes, and the deviatoric stress, which accounts for shape changes (see Figure 2.1).

Therefore, the V-Biomech uses the u/P formulation, which is a well-known mixed method, allowing the evaluation of mechanical behaviour of incompressible or nearly incompressible materials. This mixed approach uses a two-field manner, where the displacement  $\mathbf{u}$  and the pressure  $p$  are independent variables. The name of mixed u/P formulation reflects the use of separate interpolations for the displacements and the Cauchy (hydrostatic) pressure.

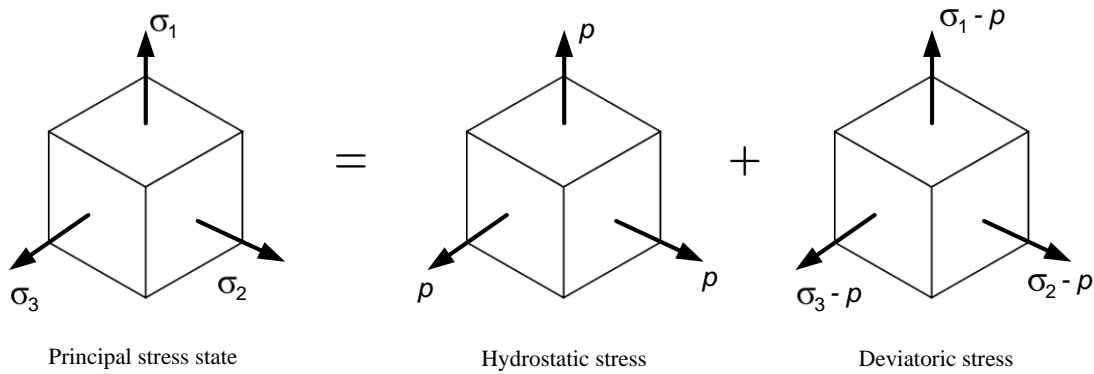


**Figure 2.1.** Stress decomposition scheme into hydrostatic and deviatoric contributions.

### 2.3. Finite strain theory

In continuum mechanics, the finite strain theory is used to describe large deformations of a solid body [8][9]. In this case, the total displacement is seen as two different components: rigid-body displacement and deformation. In order to track the behaviour of a solid body, there is a need for some material coordinates that describe its movement. Thus, the displacement is defined by:

$$\mathbf{x}(\mathbf{X}, t) = \mathbf{X} + \mathbf{u}(\mathbf{X}, t), \quad (2.1)$$

where  $\mathbf{X}$  represents the initial position,  $\mathbf{x}$  the position in a time instant  $t$ , and  $\mathbf{u}$  displacement vector. Another important concept is the deformation gradient tensor  $\mathbf{F}$ , which describes the body's local deformation allowing to relate the two configurations (initial and actual) independently of its rigid-body displacement:

$$\mathbf{F}(\mathbf{X}, t) = \frac{\partial \mathbf{x}}{\partial \mathbf{X}} = \frac{\partial \mathbf{X} + \mathbf{u}(\mathbf{X}, t)}{\partial \mathbf{X}} = \mathbf{I} + \frac{\partial \mathbf{u}}{\partial \mathbf{X}} \quad (2.2)$$

Notice that the deformation gradient tensor can also describe the Jacobian, which is a measure of the local volume change:

$$J = \det(\mathbf{F}) \quad (2.3)$$

In order to define deformations in the reference configuration, the right Cauchy-Green deformation tensor  $\mathbf{C}$  is adopted, which is defined by:

$$\mathbf{C} = \mathbf{F}^T \mathbf{F} = \mathbf{U}^2 \quad (2.4)$$

where  $\mathbf{U}$  denotes the right stretch tensor. The eigenvalues of the right stretch tensor  $\mathbf{U}$  are the principal stretches  $\lambda_i$  and the eigenvalues of the right Cauchy-Green tensor  $\mathbf{C}$  are the squares of the principal stretches,  $\lambda_i^2$ . The invariants of  $\mathbf{C}$  are often used in the expressions for strain energy density functions. Accordingly, the invariants of  $\mathbf{C}$  are defined by:

$$I_1 = \text{tr}(\mathbf{C}) = \mathbf{C} : \mathbf{I} = \lambda_1^2 + \lambda_2^2 + \lambda_3^2 \quad (2.5)$$

$$I_2 = \frac{1}{2} (I_1^2 - \mathbf{C} : \mathbf{C}) = \lambda_1^2 \lambda_2^2 + \lambda_2^2 \lambda_3^2 + \lambda_3^2 \lambda_1^2 \quad (2.6)$$

$$I_3 = \det(\mathbf{C}) = \lambda_1^2 \lambda_2^2 \lambda_3^2 \quad (2.7)$$

where the third invariant becomes equal to 1 for incompressible materials, since  $I_3 = \det(\mathbf{C}) = [\det(\mathbf{F})]^2 = J^2 = 1$ , which represents the total volume changes.

For nearly incompressible materials it is necessary to define volumetric  $\left(j^{\frac{1}{3}} \mathbf{I}\right)$  and deviatoric  $\left(\bar{\mathbf{F}} = j^{-\frac{1}{3}} \mathbf{F}\right)$  parts of the deformation gradient [10], as illustrated in Figure 2.2. Therefore, total deformation gradient tensor can be rewritten as:

$$\mathbf{F} = \left(j^{\frac{1}{3}} \mathbf{I}\right) \times \left(j^{-\frac{1}{3}} \mathbf{F}\right) = \left(j^{\frac{1}{3}} \mathbf{I}\right) \bar{\mathbf{F}} \quad (2.8)$$

which is multiplicatively separated into a volumetric part  $\left(j^{\frac{1}{3}} \mathbf{I}\right)$  and an incompressible deviatoric contribution, where  $\det(\mathbf{F}) = J$  and  $\det(\bar{\mathbf{F}}) = 1$ .

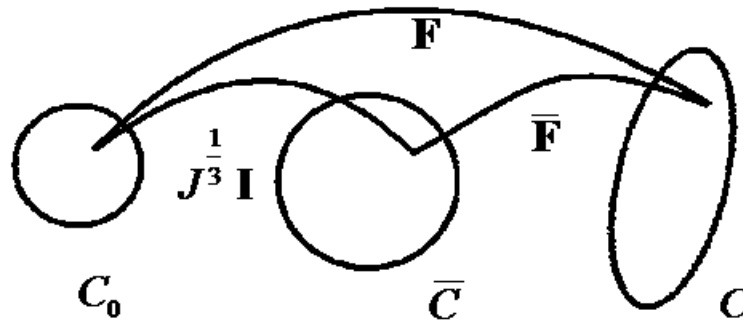


**Figure 2.2.** Decomposition of deformation gradient tensor into volumetric and deviatoric components.

Taking into account the decomposition presented in equation (2.8), the same multiplicative decomposition can be applied to  $\mathbf{F}$ ,  $\mathbf{C}$  and  $\mathbf{E}$ , allowing to obtain measures of the modified right Cauchy-Green strain tensor:

$$\bar{\mathbf{C}} = (\bar{\mathbf{F}})^T \bar{\mathbf{F}} = J^{-\frac{2}{3}} \mathbf{C} \quad (2.9)$$

The principal invariants of the deviatoric right Cauchy-Green tensor  $\bar{\mathbf{C}}$  are related to the principal invariants of the right Cauchy-Green tensor by the following relationships:

$$\bar{I}_1 = J^{-\frac{2}{3}} I_1 = \bar{\mathbf{C}} : \mathbf{I} \quad (2.10)$$

$$\bar{I}_2 = J^{-\frac{4}{3}} I_2 = \frac{1}{2} (I_1^2 - \bar{\mathbf{C}} : \bar{\mathbf{C}}) \quad (2.11)$$

$$\bar{I}_3 = \det(\bar{\mathbf{F}}) = 1 \quad (2.12)$$

For uniaxial stress state, the stretch notation can be particularly useful since the stretches can be directly calculated from the initial and final body geometry. The Green-Lagrange tensor is also easily defined with a given  $\mathbf{C}$  by:

$$\mathbf{E} = \frac{1}{2} (\mathbf{C} - \mathbf{I}) = \frac{1}{2} (\mathbf{U}^2 - \mathbf{I}) \quad (2.13)$$

which is one of the many outputs generated by the V-Biomech when analysing a Gauss point. Furthermore, the values of the three principal stretches  $\lambda_i$  can be evaluated in all increments for any predefined Gauss point.

Another useful output information, in all increments for any predefined Gauss point, is the stress tensors provided by the finite element code: the Cauchy stress tensor  $\boldsymbol{\sigma}$  and the second Piola-Kirchhoff tensor  $\boldsymbol{\Pi}$ . The first Piola-Kirchhoff tensor  $\mathbf{P}$  can be easily calculated through the Cauchy stress tensor by:

$$\mathbf{P} = J \boldsymbol{\sigma} \mathbf{F}^{-T} \quad (2.14)$$

and represents the ratio between the force in the deformed configuration and the non-deformed area, while the second Piola-Kirchhoff tensor  $\boldsymbol{\Pi}$  is defined by the force recalculated in the non-deformed configuration in the non-deformed area, which can be obtained by:

$$\boldsymbol{\Pi} = J \mathbf{F}^{-1} \boldsymbol{\sigma} \mathbf{F}^{-T} = \mathbf{F}^{-1} \mathbf{P} \quad (2.15)$$

Moreover, the Cauchy stress tensor can be related to the second Piola-Kirchhoff tensor by:

$$\boldsymbol{\sigma} = J^{-1} \mathbf{F} \boldsymbol{\Pi} \mathbf{F}^T \quad (2.16)$$



### 3. CONSTITUTIVE MODEL FOR RUBBER LIKE MATERIALS

#### 3.1. Hyperelasticity

The linear relationship between stress and strain, observed in the elastic regime of metallic materials, is not present in rubber-like materials. In fact, they display a non-linear elastic behaviour for large values of deformation, which is usually described through a hyperelastic constitutive model based on a strain energy density function. Figure 3.1 shows that the hyperelastic material only presents a linear behaviour for small strains and non-linear behaviour for large strains. The most common examples for this kind of behaviour are rubber-like materials, filled and unfilled vulcanized elastomers, biological tissues and foams.

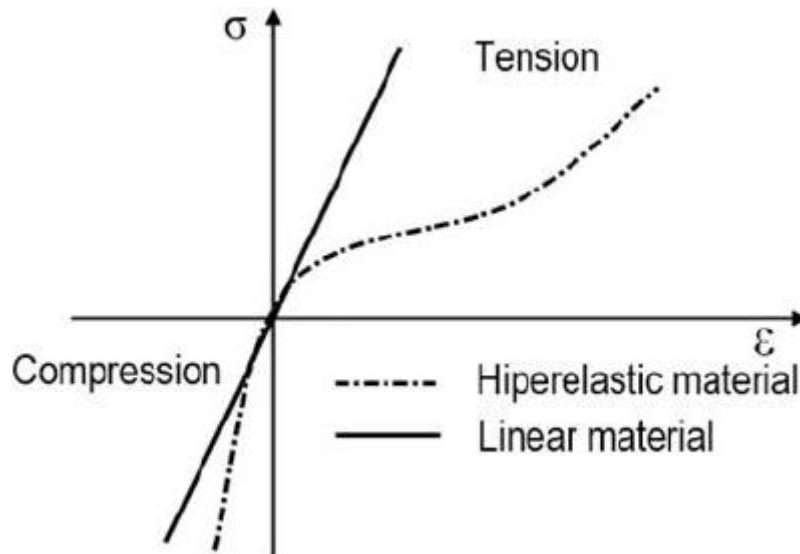


**Figure 3.1.** Comparison between linear and non-linear stress – strain curves in elastic domain.

Throughout this study, focus will be given to studying rubber materials with nearly incompressible and incompressible behaviour, therefore a great resistance to volume changes. The bulk and shear modulus can be described by the following expressions:

$$K = \frac{E}{3(1 - 2\nu)} \quad (3.1)$$

$$G = \frac{E}{2(1 + \nu)} \quad (3.2)$$

### 3.1.1. Strain Energy Function

In a hyperelastic framework, there is a need for postulating the existence of a strain energy function  $W(\mathbf{C})$ , defined per unit of reference volume, which is used in the definition of the second Piola-Kirchhoff stress tensor [11]. Considering isotropic hyperelastic materials, the strain energy function can be written in terms of the principal invariants of  $\mathbf{C}$ :

$$W(\mathbf{C}) = W(I_1, I_2, I_3) \quad (3.3)$$

The strain energy function can be defined by its 3 parts: total deviatoric strain energy, volumetric strain energy and the pressure balance that couples the mixed formulation:

$$W(\mathbf{C}) = \bar{W}(\bar{\mathbf{C}}) + \bar{W}_H(J) + Q^0(J) \quad (3.4)$$

$$W(\mathbf{C}) = \bar{W}(\bar{\mathbf{C}}) + \frac{K}{2}(J - 1)^2 - \frac{1}{2K}(\bar{p} - \tilde{p})^2 \quad (3.5)$$

where  $K$  is the initial and constant Bulk Modulus of the material,  $\bar{p}$  is the pressure computed from the displacement field ( $\bar{W}(\bar{\mathbf{C}})$ ) and  $\tilde{p}$  is the interpolated pressure from the pressure field, which is connected to the pressure degree of freedom associated with the u/P method.

### 3.1.2. Mooney-Rivlin constitutive model

In order to describe the strain energy density function, several constitutive models were developed, such as:

1. Neo-Hookean
2. Mooney-Rivlin
3. Yeoh
4. Ogden
5. Arruda-Boyce
6. Humphrey

A comparative study of several constitutive models was made by Martins et al [12] using the uniaxial tension conditions of a silicone-rubber sample. Figure 3.2 presents the comparison between the experimental and the stress-stretch curves obtained by each model. Although most of the models capture accurately the experimental trend, the Neo-Hookean model falls short on predicting the experimental behaviour, which would be expected since it is the simplest model (only one material parameter).

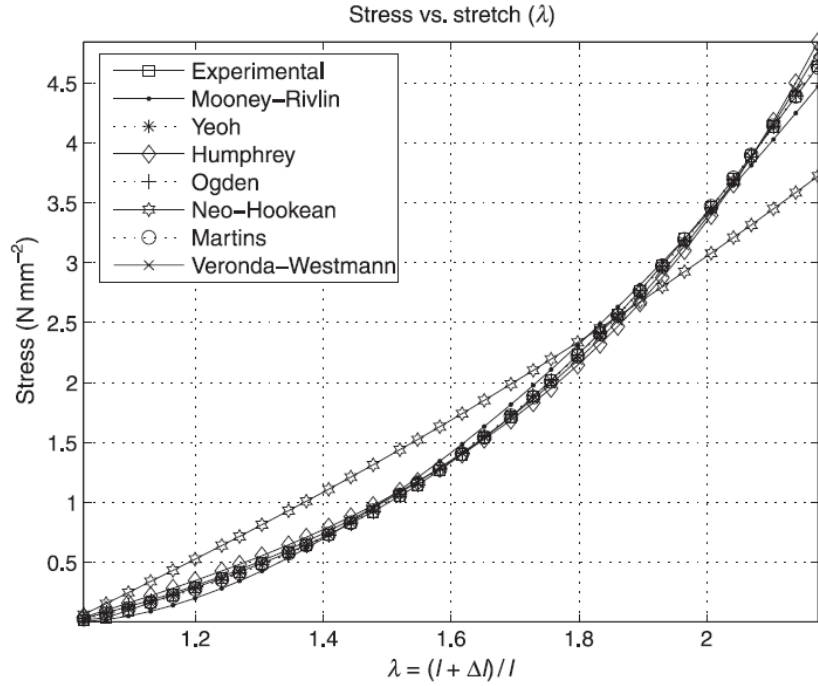


**Figure 3.2.** Comparison between experimental and numerical results of stress-stretch curves under uniaxial tension conditions for silicone-rubber material [12].

Several experimental studies showed that the Mooney-Rivlin model is especially adequate for modelling the rubber behaviour [13][14]. Moreover, due to its simplicity, it is the constitutive model adopted in this study. Its general equation for the strain potential is given by:

$$\bar{W}_{MR}(\bar{\mathbf{C}}) = \sum_{i+j=1}^N C_{ij}(\bar{I}_1 - 3)^i(\bar{I}_2 - 3)^j \quad (3.6)$$

and if  $N = 1$  (two material parameters), then:

$$\bar{W}_{MR}(\bar{\mathbf{C}}) = C_{10}(\bar{I}_1 - 3) + C_{01}(\bar{I}_2 - 3) \quad (3.7)$$

where  $C_{10}$  and  $C_{01}$  are the material parameters. Although two parameters ( $N = 1$ ) seems to be enough to characterize some rubbers, more parameters are required if the stress-stretch curve presents one or two inflexion points [15]. Moreover, equation (3.6) can also deduce the Polynomial for  $N = 2$ , where Mooney-Rivlin constitutive model uses 5 parameters with  $C_{11}$ ,  $C_{20}$  and  $C_{02}$  as additional parameters:

$$\begin{aligned} \bar{W}_{MR}(\bar{\mathbf{C}}) = & C_{10}(\bar{I}_1 - 3) + C_{01}(\bar{I}_2 - 3) + C_{11}(\bar{I}_1 - 3)(\bar{I}_2 - 3) \\ & + C_{20}(\bar{I}_1 - 3)^2 + C_{02}(\bar{I}_2 - 3)^2 \end{aligned} \quad (3.8)$$

### 3.1.3. Stress evaluation: second Piola-Kirchhoff

The second Piola-Kirchhoff stress tensor is commonly adopted to describe the hyperelastic behaviour, not due to its definition but because it can be derived from the relation:

$$\mathbf{\Pi} = \frac{\partial W}{\partial \mathbf{E}} \quad (3.9)$$

which can be written in terms of the right Cauchy-Green deformation tensor:

$$\mathbf{\Pi} = 2 \frac{\partial W}{\partial \mathbf{C}} \quad (3.10)$$

Notice that, in order to calculate the second Piola-Kirchhoff tensor, the pressure balance parcel should be ignored, since at the equilibrium the average pressure should be equal to the interpolated pressure. Thus, giving the following expression:

$$\bar{\Pi}_{kl} = 2 \frac{\partial [\bar{W}(\bar{\mathbf{C}}) + \bar{W}_H(J)]}{\partial C_{kl}} \quad k, l = 1, 2, 3 \quad (3.11)$$

The partial derivative of the volumetric strain energy with respect to right Cauchy-Green deformation tensor is:

$$\frac{\partial \bar{W}_H(J)}{\partial C_{kl}} = \frac{\partial \left( \frac{k}{2} (J - 1)^2 \right)}{\partial C_{kl}} = \frac{K}{2} J (J - 1) C_{kl}^{-1} \quad k, l = 1, 2, 3 \quad (3.12)$$

which can be related to the average pressure,  $\bar{p}(=\tilde{p})$ , that, after some mathematical developments by Alves et al [6], was found to be equal to the hydrostatic pressure of the Cauchy tensor:

$$\bar{p} = -K (J - 1) \quad (3.13)$$

However, the other partial derivative depends on the constitutive model adopted. Thus, considering the Mooney-Rivlin model defined by equation (3.7) with two parameters, the first partial derivative of the Strain Potential is:

$$\frac{\partial \bar{W}(\bar{\mathbf{C}})}{\partial C_{kl}} = \frac{\partial \bar{W}_{MR}(\bar{\mathbf{C}})}{\partial \bar{I}_1} \frac{\partial \bar{I}_1}{\partial C_{kl}} + \frac{\partial \bar{W}_{MR}(\bar{\mathbf{C}})}{\partial \bar{I}_2} \frac{\partial \bar{I}_2}{\partial C_{kl}} \quad k, l = 1, 2, 3 \quad (3.14)$$

with:

$$\frac{\partial \bar{I}_1}{\partial C_{kl}} = \left( -\frac{1}{3} J^{-\frac{2}{3}} I_1 \right) C_{kl}^{-1} + J^{-\frac{2}{3}} \delta_{kl} \quad k, l = 1, 2, 3 \quad (3.15)$$

$$\frac{\partial \bar{I}_2}{\partial C_{kl}} = \left( -\frac{2}{3} J^{-\frac{4}{3}} I_2 \right) C_{kl}^{-1} + J^{-\frac{4}{3}} \frac{\partial I_2}{\partial C_{kl}} \quad k, l = 1, 2, 3 \quad (3.16)$$

$$\frac{\partial I_2}{\partial C_{kl}} = I_1 \delta_{kl} - C_{kl} \quad k, l = 1, 2, 3 \quad (3.17)$$

and:

$$\frac{\partial \bar{W}_{MR}(\bar{\mathbf{C}})}{\partial \bar{I}_1} = \sum_{i+j=1}^1 C_{ij} i (\bar{I}_1 - 3)^{i-1} (\bar{I}_2 - 3)^j = C_{10} \quad i, j = 1 \quad (3.18)$$

$$\frac{\partial \bar{W}_{MR}(\bar{\mathbf{C}})}{\partial \bar{I}_2} = \sum_{i+j=1}^1 C_{ij} j (\bar{I}_1 - 3)^i (\bar{I}_2 - 3)^{j-1} = C_{01} \quad i, j = 1 \quad (3.19)$$

Assembly all parcels into only one, the second Piola-Kirchhoff stress tensor is given by:

$$\begin{aligned} \bar{\Pi}_{kl} = 2 \left\{ \left[ \left( -\frac{1}{3} J^{-\frac{2}{3}} I_1 \right) C_{kl}^{-1} + J^{-\frac{2}{3}} \delta_{kl} \right] C_{10} + \left[ \left( -\frac{2}{3} J^{-\frac{4}{3}} I_2 \right) C_{kl}^{-1} + J^{-\frac{4}{3}} (I_1 \delta_{kl} - \right. \right. \\ \left. \left. C_{kl}) \right] C_{01} + \frac{k}{2} J (J - 1) C_{kl}^{-1} \right\} \quad k, l = 1, 2, 3 \end{aligned} \quad (3.20)$$

### 3.1.4. Uniaxial stress state under incompressible conditions

Since the identification of the material parameters required for the constitutive models are usually obtained from simple experimental mechanical tests, the uniaxial extension of a test cube is considered in this section, as shown in Figure 3.3. The objective is to obtain a uniaxial stress state, which is present in the uniaxial tensile/compression tests. Besides, in order to simplify the stress evaluation, the material is assumed total incompressible.

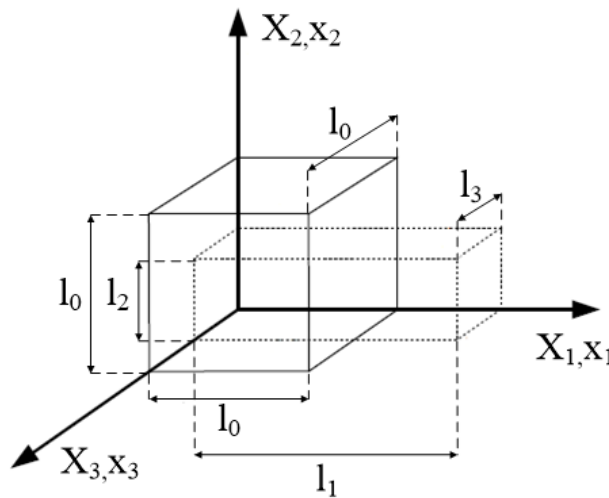


**Figure 3.3.** Initial and final configuration of a cube under uniaxial traction along  $x_1$  direction.

Taking into account the cube length in each direction before and after loading, the stretch can be evaluated in each direction using the coordinate transformation given by  $x_i = \lambda_i X_i$ . Since the loading is performed along a global axis, the obtained stretch values are also the principal stretches  $\lambda_i$ . Assuming uniaxial traction along direction  $\mathbf{x}_1$  and incompressible isotropic material, the corresponding stretches are:

$$\begin{aligned}\lambda_1 &= \lambda \\ \lambda_2 &= \lambda^{-\frac{1}{2}} \\ \lambda_3 &= \lambda^{-\frac{1}{2}}\end{aligned}\tag{3.21}$$

The deformation gradient tensor and the right Cauchy-Green deformation tensor are obtained using equation (2.2) and (2.4), respectively:

$$\mathbf{F} = \begin{bmatrix} \lambda & 0 & 0 \\ 0 & \lambda^{-\frac{1}{2}} & 0 \\ 0 & 0 & \lambda^{-\frac{1}{2}} \end{bmatrix}\tag{3.22}$$

$$\mathbf{C} = \begin{bmatrix} \lambda & 0 & 0 \\ 0 & \lambda^{-\frac{1}{2}} & 0 \\ 0 & 0 & \lambda^{-\frac{1}{2}} \end{bmatrix} \begin{bmatrix} \lambda & 0 & 0 \\ 0 & \lambda^{-\frac{1}{2}} & 0 \\ 0 & 0 & \lambda^{-\frac{1}{2}} \end{bmatrix} = \begin{bmatrix} \lambda^2 & 0 & 0 \\ 0 & \lambda^{-1} & 0 \\ 0 & 0 & \lambda^{-1} \end{bmatrix}\tag{3.23}$$

Since the obtained right Cauchy-Green deformation tensor is a diagonal matrix, the invariants of  $\mathbf{C}$  are simply defined through the principal stretches using equations (2.5), (2.6) and (2.7):

$$\begin{aligned}I_1 &= \lambda^2 + 2\lambda^{-1} \\ I_2 &= 2\lambda + \lambda^{-2} \\ I_3 &= \lambda^2 \lambda^{-1} \lambda^{-1} = 1\end{aligned}\tag{3.24}$$

Considering the incompressibility assumption, equation (3.14) can be simplified to calculate the component of the second Piola-Kirchhoff stress tensor in the loading direction connected with the constitutive model, where  $C_{11}^{-1} = \lambda^{-2}$ . Thus, resulting in:

$$\begin{aligned}\frac{\partial \bar{W}(\bar{\mathbf{C}})}{\partial C_{11}} &= \left[ -\frac{1}{3} (\lambda^2 + 2\lambda^{-1})\lambda^{-2} + 1 \right] C_{10} \\ &+ \left[ -\frac{2}{3} (2\lambda + \lambda^{-2})\lambda^{-2} + (\lambda^2 + 2\lambda^{-1} - \lambda^2) \right] C_{01} \\ &= \frac{2}{3} (C_{10}\lambda + C_{01})(\lambda^{-1} - \lambda^{-4})\end{aligned}\tag{3.25}$$

which relates the elastic potential with the principal stretch. The volumetric part of the second Piola-Kirchhoff stress tensor requires for more complex analysis. In [16] it is suggested to take in consideration the following decomposition of the Cauchy stress tensor:

$$\boldsymbol{\sigma} = \mathbf{s} + \mathbf{p} \quad (3.26)$$

where  $\mathbf{s} = \text{dev}[\boldsymbol{\sigma}]$  is the deviatoric stress component, whereas  $\mathbf{p} = \text{hyd}[\boldsymbol{\sigma}]$  is the hydrostatic part of the stress tensor. In this case the deviatoric stress can be seen as the constitutive model part, already simplified on equation (3.25), and the hydrostatic part as the volumetric strain energy part that has not been simplified yet. Both components can be further decomposed:

$$\mathbf{p} = \frac{1}{3} \text{tr}(\boldsymbol{\sigma}) \mathbf{I} \quad (3.27)$$

$$\mathbf{s} = \boldsymbol{\sigma} - \mathbf{p} \quad (3.28)$$

In case of uniaxial stress state the hydrostatic component is obtained from the zero transverse stress constrain, i.e.  $\sigma_{22} = \sigma_{33} = 0$ , which implies:

$$\boldsymbol{\sigma} = \begin{bmatrix} \sigma & 0 & 0 \\ 0 & 0 & 0 \\ 0 & 0 & 0 \end{bmatrix} \quad (3.29)$$

Consequently, both deviatoric and hydrostatic parts can be rewritten as:

$$s_{11} = \sigma_{11} - \frac{1}{3} \sigma_{11} = \frac{2}{3} \sigma_{11} \quad (3.30)$$

$$p_{11} = \frac{1}{3} \sigma_{11} = \frac{s_{11}}{2} \quad (3.31)$$

which shows that the hydrostatic part is half value of the deviatoric part, meaning that  $\boldsymbol{\sigma} = \frac{3}{2} \mathbf{s}$  for the actual conditions. Accordingly, by joining equation (3.25) and (3.31), the second Piola-Kirchhoff component is defined as:

$$\Pi_{11} = 2(C_{10}\lambda + C_{01})(\lambda^{-1} - \lambda^{-4}) \quad (3.32)$$

Furthermore, this relationship can give information about other stress tensors like the first Piola-Kirchhoff and the Cauchy stress tensor. From equations (2.14) and (2.15) it is possible to establish a clear relation between those tensors for the principal stretch direction 11:

$$\sigma_{11} = P_{11} \lambda = \frac{\Pi_{11} \lambda^2}{J} \quad (3.33)$$

Notice that in order to assume incompressibility  $J = 1$ . This relation is used to obtain different stress quantities in the principal stress direction, which are listed in Table 3.1.

**Table 3.1.** Component of the stress tensors in the loading direction considering the Mooney-Rivlin constitutive model with 2 parameters.

	Stress component
Cauchy Stress	$\sigma_{11} = 2(C_{10}\lambda + C_{01})(\lambda - \lambda^{-2})$
1st Piola Kirchhoff	$P_{11} = 2(C_{10}\lambda + C_{01})(1 - \lambda^{-3})$
2nd Piola Kirchhoff	$\Pi_{11} = 2(C_{10}\lambda + C_{01})(\lambda^{-1} - \lambda^{-4})$

The first Piola-Kirchhoff tensor can also be calculated by:

$$\frac{\partial \bar{W}_{MR}}{\partial \lambda} = 2(C_{10}\lambda + C_{01})(1 - \lambda^{-3}) \quad (3.34)$$

which implies that, considering equation (3.33), the second Piola-Kirchhoff stress component in the loading direction can be easily obtained by:

$$\Pi_{11} = \frac{\partial \bar{W}_{MR}}{\partial \lambda} \frac{1}{\lambda} = 2(C_{10}\lambda + C_{01})(\lambda^{-1} - \lambda^{-4}) \quad (3.35)$$

Bearing this in mind and remembering equation (3.6), it is easy to extract the same Mooney-Rivlin conclusions for 5 parameters (see Table 3.2).

**Table 3.2.** Component of the second Piola Kirchhoff stress tensor in the loading direction considering the Mooney-Rivlin constitutive model with 2 and 5 parameters.

	Mooney-Rivlin 2nd Piola Kirchhoff
2 parameters	$\Pi_{11} = 2(C_{10}\lambda + C_{01})(\lambda^{-1} - \lambda^{-4})$
5 parameters	$\begin{aligned} \Pi_{11} = & 2(C_{10}\lambda + C_{01})(\lambda^{-1} - \lambda^{-4}) \\ & + 6\lambda^{-1}(\lambda^2 - \lambda - 1 + \lambda^{-2} + \lambda^{-3} - \lambda^{-4})C_{11} \\ & + 4\lambda^{-1}(\lambda^3 - 3\lambda + 1 + 3\lambda^{-2} - 2\lambda^{-3})C_{20} \\ & + 4\lambda^{-1}(-\lambda^{-5} + 2\lambda - 3 - \lambda^{-2} + 3\lambda^{-3})C_{20} \end{aligned}$

### 3.2. Viscoelasticity

The time dependent deformation exhibited by the rubbers is described by the viscoelasticity. In order to describe this behaviour, the hyper-viscoelastic formulation can be represented by a rheological analogy – the generalized Maxwell model, represented in Figure 3.4. The generalized Maxwell model is composed by an elastic spring related to the



hyperelastic part, and a finite number of Maxwell elements that describe the viscoelasticity. Furthermore, each Maxwell element is composed by an elastic spring and a viscous Newton-element.

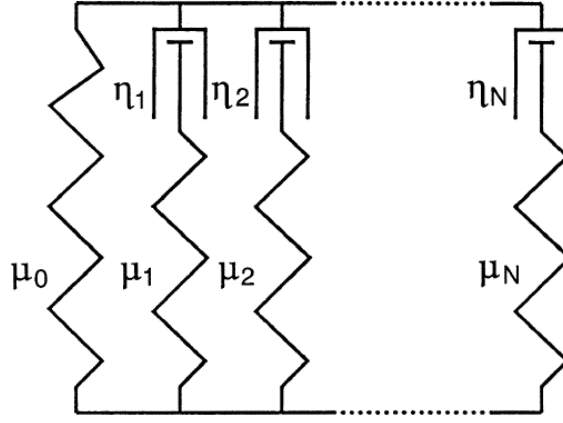


**Figure 3.4.** Rheological analogy approach representing the generalized Maxwell model.

The deduction of the viscoelastic stress was first presented by Kaliske et al [17] and is given by:

$$h_j^{n+1} = \exp\left(-\frac{\Delta t}{\tau_j}\right) h_j^n + ak_j \frac{1 - \exp\left(-\frac{\Delta t}{\tau_j}\right)}{\frac{\Delta t}{\tau_j}} [\sigma_0^{n+1} - \sigma_0^n] \quad (3.36)$$

where  $h_j^{n+1}$  represents the viscoelastic stress at increment  $n+1$ , while  $\sigma_0^{n+1}$  denotes the stress imposed by the hyperelastic behaviour. Furthermore,  $ak_j$  and  $\tau_j$  are parameters related to the  $j$  Maxwell element, used to describe its behaviour. This phenomenon is described in V-Biomech by using as inputs the relaxation time  $\tau$  and the ratio:

$$ak_j = \frac{\mu_j}{\mu_0} \quad (3.37)$$

where  $\mu_j$  denotes the  $j$  Maxwell element spring elastic constant, whereas  $\mu_0$  is related to the hyperelastic spring elastic constant. The stress relaxation is given by the following equation and its relaxation function:

$$\hat{\sigma}(t) = \mu_0 \hat{\epsilon}(0) + \sum_{j=1}^M \mu_j \exp\left(-\frac{t}{\tau_j}\right) \hat{\epsilon}(0) = \hat{\Gamma}(t) \hat{\epsilon}(0) \quad (3.38)$$

$$\hat{\Gamma}(t) = \mu_0 + \sum_{j=1}^M \mu_j \exp\left(-\frac{t}{\tau_j}\right) \quad (3.39)$$

where  $M$  denotes the number of Maxwell elements. The relaxation function can be represented in its normalized form:

$$\hat{\gamma}(t) = \frac{\hat{\Gamma}(t)}{\mu_0} = 1 + \sum_{j=1}^M ak_j \exp\left(-\frac{t}{\tau_j}\right) \quad (3.40)$$

### 3.3. Hyper-viscoelasticity

The accurate description of the rubber behaviour requires two types of formulations: hyperelasticity and viscoelasticity. Furthermore, the viscoelasticity is also dependent from the hyperelasticity. The generalized Maxwell element provides an organized vision of the mechanical behaviour, defining both contributions together. Consequently, the second Piola-Kirchhoff stress tensor, evaluated in a given increment, is given by the sum of two components, specifically the stress produced by the hyperelastic behaviour ( $\Pi_{HE}$ ) and the stress generated by each Maxwell element ( $\Pi_{MW_i}$ ) given by equation (3.36):

$$\Pi_{total} = \Pi_{HE} + \sum_{i=1}^M \Pi_{MW_i} \quad (3.41)$$

where the stress under each Maxwell element at the increment  $n+1$  is:

$$\Pi_{MW_i}^{n+1} = \exp\left(-\frac{\Delta t}{\tau_i}\right) \Pi_{MW_i}^n + \frac{ak_i \tau_i}{\Delta t} \left[1 - \exp\left(-\frac{\Delta t}{\tau_i}\right)\right] (\Pi_{HE}^{n+1} - \Pi_{HE}^n) \quad (3.42)$$

and considering  $\Delta t$  the respective time increment.

#### 3.3.1. Viscoelasticity modes in V-Biomech

Since the viscoelasticity component of the Maxwell model takes into account the hyperelastic behaviour (Mooney-Rivlin), two different approaches can be adopted in the V-Biomech finite element code. By accessing the (Mater1 file), the user can change the viscoelastic mode by changing the option “viscousLONG”, which will change the meaning of  $\sigma_0^{n+1}$  and  $\sigma_0^n$  in equation (3.36). In this study, mode I and mode III will be addressed. The mode I considers only the deviatoric stress component from the hyperelastic behaviour when calculating the viscoelastic part:

$$\bar{\Pi}_{kl} = 2 \frac{\partial \bar{W}(\bar{\mathbf{C}})}{\partial \bar{C}_{kl}} \quad (3.43)$$

which is the formulation used by Abaqus. On the other hand, adopting the mode III both hydrostatic and deviatoric stress components resulting from the hyperelasticity are taken into account:

$$\bar{\Pi}_{kl} = 2 \frac{\partial [\bar{W}(\bar{\mathbf{C}}) + \bar{W}_H(J)]}{\partial C_{kl}} \quad (3.44)$$

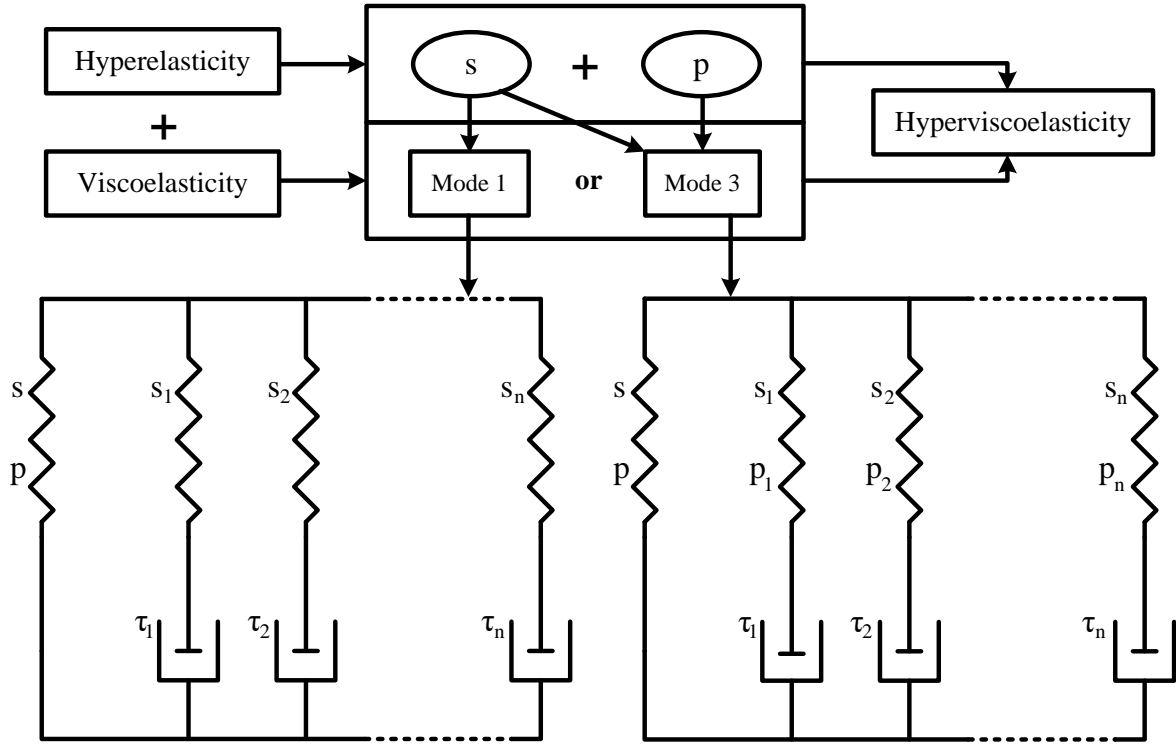


**Figure 3.5.** Scheme drawing of the 2 V-Biomech modes that sums the mechanical behaviour of each one.

Figure 3.5 presents schematically the workflow used to evaluate the total stress in mode I and mode III of the V-Biomech. The mode III uses equation (3.31) as an assumption, making the relationship between the deviatoric and hydrostatic stress components of the hyperelastic behaviour constant. On the other hand, in the mode I, the relationship between the deviatoric and hydrostatic stress components is neither constant or linear.

Considering the mode III, both deviatoric and hydrostatic stress components are taken into account in the calculations for the Maxwell element stress. Thus, the ratio between the stress components is constant in all Maxwell branches, therefore expanding the relation and keeping it constant in all system. However, in the mode I, only the deviatoric stress component enters in the calculation for the Maxwell element stress. Therefore, the only hydrostatic stress component in the system (dictated only by the hyperelasticity), which must

guarantee zero transverse stress, must balance the deviatoric stress components of all Maxwell elements.

### 3.3.2. Mode I: uniaxial compression

In order to analyse the contribution of the hydrostatic and deviatoric stress components, the instantaneous uniaxial compression with relaxation afterwards is studied considering only one Maxwell element. Therefore, the total system stress can be written as:

$$\sigma_{total} = s + p + s_1 \quad (3.45)$$

where the deviatoric stress component of the Maxwell element ( $s_1$ ) can be defined as a function of the deviatoric stress component given by the Mooney-Rivlin (hyperelasticity):

$$s_1 = s \left( ak_1 \exp\left(\frac{-t}{\tau_1}\right) \right) \quad (3.46)$$

In order to satisfy the zero-transverse condition, the ratio between the total system deviatoric stress component,  $s_{total}$ , and the hydrostatic stress should be:

$$\frac{s_{total}}{p} = \frac{s + s_1}{p} = 2 \quad (3.47)$$

Accordingly, the hydrostatic stress component is:

$$\begin{aligned} \frac{\sigma_{total}}{p} = \frac{s + p + s_1}{p} &\Leftrightarrow \frac{s_{total}}{p} = \frac{s + s_1}{p} \Leftrightarrow 2 = \frac{s \left( 1 + ak_1 \exp\left(\frac{-t}{\tau_1}\right) \right)}{p} \\ p &= \frac{s \left( 1 + ak_1 \exp\left(\frac{-t}{\tau_1}\right) \right)}{2} \end{aligned} \quad (3.48)$$

Since the deviatoric stress component can be easily calculated assuming material incompressibility, the pressure is given by equation (3.48) in the relaxation test (constant value of stretch during the time).

In order to establish a relationship between the hydrostatic and the deviatoric stress components during the uniaxial compression at constant speed of prescribed displacement, the deviatoric Maxwell stress is defined as a function of the hyperelastic deviatoric stress. The total stress is calculated using equation (3.41), which is described recursively for each increment:

$$\begin{aligned}
 \sigma_s^n &= \sigma_{HE}^n + \exp\left(\frac{-\Delta t}{\tau_i}\right) \sigma_{MW}^{n-1} + \frac{ak\tau}{\Delta t} \left[1 - \exp\left(\frac{-\Delta t}{\tau}\right)\right] (\sigma_{HE}^n - \sigma_{HE}^{n-1}) = \\
 &= s_{HE}^n \left[1 + \frac{ak\tau}{\Delta t} \left(1 - \exp\left(\frac{-\Delta t}{\tau}\right)\right)\right] + \exp\left(\frac{-\Delta t}{\tau}\right) \sigma_{MW}^{n-1} + p_{HE}^n + \\
 &s_{HE}^{n-1} \left[\frac{ak\tau}{\Delta t} \left(\exp\left(\frac{-\Delta t}{\tau}\right) - 1\right)\right]
 \end{aligned} \tag{3.49}$$

Notice that the total stress component from the hyperelasticity on the actual increment,  $\sigma_{HE}^n$ , can be divided into two different parts: deviatoric stress ( $s_{HE}^n$ ) and hydrostatic stress ( $p_{HE}^n$ ). Moreover, the total Maxwell stress of the previous increment,  $\sigma_{MW}^{n-1}$ , only a deviatoric component (mode I). Considering equation (3.49), the total system stress in the current increment,  $\sigma_s^n$ , can be defined as a function of only the hyperelastic part, i.e. the deviatoric Maxwell stress defined as a function of the hyperelastic deviatoric stress.

The explicit expressions for the total stress in three consecutive increments is given in the following, using only the stress component from the hyperelasticity:

- For  $n = 0 \rightarrow s_{HE}^0 = 0 \rightarrow \sigma_s^0 = 0$
- For  $n = 1 \rightarrow s_{HE}^0 = \sigma_{MW}^0 = 0 \rightarrow \sigma_s^1 = s_{HE}^1 \left[1 + \frac{ak\tau}{\Delta t} \left(1 - \exp\left(\frac{-\Delta t}{\tau}\right)\right)\right] + p_{HE}^1$
- For  $n = 2 \rightarrow \sigma_{MW}^1 = s_{HE}^1 \left[\frac{ak\tau}{\Delta t} \left(1 - \exp\left(\frac{-\Delta t}{\tau}\right)\right)\right] \rightarrow \sigma_s^2 = s_{HE}^2 \left[1 + \frac{ak\tau}{\Delta t} \left(1 - \exp\left(\frac{-\Delta t}{\tau}\right)\right)\right] + p_{HE}^2 + \exp\left(\frac{-\Delta t}{\tau}\right) \left[\frac{ak\tau}{\Delta t} \left(1 - \exp\left(\frac{-\Delta t}{\tau}\right)\right)\right] s_{HE}^1 + s_{HE}^1 \left[\frac{ak\tau}{\Delta t} \left(\exp\left(\frac{-\Delta t}{\tau}\right) - 1\right)\right] = s_{HE}^2 \left[1 + \frac{ak\tau}{\Delta t} \left(1 - \exp\left(\frac{-\Delta t}{\tau}\right)\right)\right] + p_{HE}^2 + s_{HE}^1 \left[\frac{ak\tau}{\Delta t} \left(-1 + 2 \exp\left(\frac{-\Delta t}{\tau}\right) - \exp\left(\frac{-2\Delta t}{\tau}\right)\right)\right]$
- For  $n = 3 \rightarrow \sigma_{MW}^2 = s_{HE}^2 \left[\frac{ak\tau}{\Delta t} \left(1 - \exp\left(\frac{-\Delta t}{\tau}\right)\right)\right] + s_{HE}^1 \left[\frac{ak\tau}{\Delta t} \left(-1 + 2 \exp\left(\frac{-\Delta t}{\tau}\right) - \exp\left(\frac{-2\Delta t}{\tau}\right)\right)\right] \rightarrow \sigma_s^3 = s_{HE}^3 \left[1 + \frac{ak\tau}{\Delta t} \left(1 - \exp\left(\frac{-\Delta t}{\tau}\right)\right)\right] + p_{HE}^3 + \exp\left(\frac{-\Delta t}{\tau}\right) \left[s_{HE}^2 \left[\frac{ak\tau}{\Delta t} \left(1 - \exp\left(\frac{-\Delta t}{\tau}\right)\right)\right] + s_{HE}^1 \left[\frac{ak\tau}{\Delta t} \left(-1 + 2 \exp\left(\frac{-\Delta t}{\tau}\right) - \exp\left(\frac{-2\Delta t}{\tau}\right)\right)\right]\right] + s_{HE}^2 \left[\frac{ak\tau}{\Delta t} \left(\exp\left(\frac{-\Delta t}{\tau}\right) - 1\right)\right] = s_{HE}^3 \left[1 + \frac{ak\tau}{\Delta t} \left(1 - \exp\left(\frac{-\Delta t}{\tau}\right)\right)\right] + p_{HE}^3 + s_{HE}^2 \left[\frac{ak\tau}{\Delta t} \left(-1 + 2 \exp\left(\frac{-\Delta t}{\tau}\right) - \exp\left(\frac{-2\Delta t}{\tau}\right)\right)\right] + s_{HE}^1 \left[\frac{ak\tau}{\Delta t} \left(-\exp\left(\frac{-\Delta t}{\tau}\right) + 2 \exp\left(\frac{-2\Delta t}{\tau}\right) - \exp\left(\frac{-3\Delta t}{\tau}\right)\right)\right]$

From the pattern obtained for three increments, a general formulation based only on the deviatoric stress component from the hyperelastic can be obtained. Accordingly, two different coefficients are defined:

- A constant coefficient  $c_1$ , which is multiplied by the actual deviatoric stress component given by the hyperelastic behaviour:

$$c_1 = 1 + \frac{ak \tau}{\Delta t} \left( 1 - \exp\left(\frac{-\Delta t}{\tau}\right) \right) \quad (3.50)$$

- A second coefficient  $c_2^n$ , which depends on the increment and is associated to every previous deviatoric hyperelastic stress:

$$c_2^n = \frac{ak \tau}{\Delta t} \left( -\exp\left(\frac{-n \Delta t}{\tau}\right) + 2\exp\left(\frac{-(n-1)\Delta t}{\tau}\right) - \exp\left(\frac{-(n-2)\Delta t}{\tau}\right) \right) \quad (3.51)$$

Taking into account equation (3.50) and (3.51), the total stress of the system is given by:

$$\sigma_s^n = s_{HE}^n c_1 + p_{HE}^n + \sum_{i=1}^{n-1} s_{HE}^i c_2^{n-i+1} \quad (3.52)$$

which is still an increment dependent formulation. In order to consider several ( $M$ ) Maxwell elements these coefficients (equations (3.50) and (3.51)) should also be written in a general form, resulting in:

$$c_1 = 1 + \sum_{i=1}^M \frac{ak_i \tau_i}{\Delta t} \left( 1 - \exp\left(\frac{-\Delta t}{\tau_i}\right) \right) \quad (3.53)$$

$$c_2^n = \sum_{i=1}^M \left[ \frac{ak_i \tau_i}{\Delta t} \left( -\exp\left(\frac{-n \Delta t}{\tau_i}\right) + 2\exp\left(\frac{-(n-1)\Delta t}{\tau_i}\right) - \exp\left(\frac{-(n-2)\Delta t}{\tau_i}\right) \right) \right] \quad (3.54)$$

where the constant  $M$  denotes the total number of Maxwell elements.

In order to apply the same strategy previously adopted in the relaxation test, equation (3.52) must depend only on the deviatoric stress component from the hyperelasticity,  $s_{HE}^n$  in the actual increment. However, since the stress is highly nonlinear, it is impossible know the stress evolution from a single value in the previous increment.

Four different approaches were studied, and, from that group, one clearly stood out as being the most effective at predicting the behaviour of the hydrostatic pressure. The four suggestions will be presented and tested on the next chapter, in order to prove our choice.

1. Consider that equation (3.47) as valid to this kind of behaviour also.

2. Calculate the ratio using the sum of both coefficients. This suggestion assumes a relaxation condition which is that all the hyperelastic deviatoric stress have the same value for every increment. Therefore, leading to total stress:

$$\sigma_s^n = s_{HE}^n \left[ c_1 + \sum_{i=1}^{n-1} c_2^{n-i+1} \right] + p_{HE}^n \quad (3.55)$$

Thus, suggesting that:

$$p^n = \frac{s_{HE}^n [c_1 + \sum_{i=1}^{n-1} c_2^{n-i+1}]}{2} \quad (3.56)$$

3. Use only the first coefficient and neglect the second one:

$$p^n = \frac{s_{HE}^n c_1}{2} \quad (3.57)$$

4. Use the first coefficient  $c_1$  but with the total time instead of the increment of time:

$$p^n = \frac{s_{HE}^n \left( 1 + \sum_{i=1}^M \frac{ak_i \tau_i}{t^n} \left[ 1 - \exp\left(-\frac{t^n}{\tau_i}\right) \right] \right)}{2} \quad (3.58)$$

In this case the sum is with respect to the number of Maxwell elements,  $M$ .

Using this result, we can write the full expression for uniaxial compression, assuming material incompressibility. In this case the total second Piola-Kirchhoff should be:

$$\Pi_{total} = \Pi_{HE} + \sum_{i=1}^M \Pi_{MW_i} = s_{HE} + p_{HE} + \sum_{i=1}^M \Pi_{MW_i} \quad (3.59)$$

The hyperelastic deviatoric part is represented by equation (3.25), the hyperelastic hydrostatic part is approximated by equation (3.58), and finally the Maxwell stress is formulated by equation (3.42). Before writing the final expression, there is still some simplifications left to do in the hyperelastic part, since the deviatoric part plays a role in the hydrostatic part. Remembering equation (3.11):

$$\begin{aligned} \Pi_{HE}^n &= 2(s_{HE}^n + p^n) = 2 \left[ s_{HE}^n + \frac{s_{HE}^n \left( 1 + \sum_{i=1}^M \frac{ak_i \tau_i}{t^n} \left[ 1 - \exp\left(-\frac{t^n}{\tau_i}\right) \right] \right)}{2} \right] = s_{HE}^n \left( 3 + \right. \\ &\quad \left. \sum_{i=1}^M \frac{ak_i \tau_i}{t^n} \left[ 1 - \exp\left(-\frac{t^n}{\tau_i}\right) \right] \right) = \left[ \frac{2}{3} (C_{10}\lambda + C_{01})(\lambda^{-1} - \lambda^{-4}) \right]^n \left( 3 + \right. \\ &\quad \left. \sum_{i=1}^M \frac{ak_i \tau_i}{t^n} \left[ 1 - \exp\left(-\frac{t^n}{\tau_i}\right) \right] \right) \end{aligned} \quad (3.60)$$

It should be noted that the Maxwell stress uses only the deviatoric part of the hyperelasticity we get to the final equation that describes the total stress in second Piola-Kirchhoff:

$$\begin{aligned}\Pi_{total}^n &= \left[ \frac{2}{3} (C_{10}\lambda + C_{01})(\lambda^{-1} - \lambda^{-4}) \right]^n \left( 3 + \sum_{i=1}^M \frac{ak_i \tau_i}{t^n} \left[ 1 - \exp\left(-\frac{t^n}{\tau_i}\right) \right] \right) + \\ &\sum_{i=1}^M \exp\left(-\frac{\Delta t}{\tau_i}\right) \Pi_{MW_i}^{n-1} + \frac{ak_i \tau_i}{\Delta t} \left[ 1 - \exp\left(-\frac{\Delta t}{\tau_i}\right) \right] \left[ \left( \frac{4}{3} (C_{10}\lambda + C_{01})(\lambda^{-1} - \lambda^{-4}) \right)^n - \right. \\ &\left. \left( \frac{4}{3} (C_{10}\lambda + C_{01})(\lambda^{-1} - \lambda^{-4}) \right)^{n-1} \right]\end{aligned}\quad (3.61)$$

This expression depends only on material parameters and stretch evolution, which is ideal for the next objectives in this thesis.

### 3.3.3. Mode III: uniaxial compression

Considering the mode III, the relation between the deviatoric and hydrostatic stress components of the hyperelasticity is always constant. In section 3.1.4, it has been concluded that when the referred assumption is activated, equation (3.32) describes the total hyperelastic behaviour that also enters in the viscoelastic part, therefore leading to the following equation that reflects the total second Piola-Kirchhoff stress considering the Mooney-Rivlin constitutive model with 2 parameters:

$$\begin{aligned}\Pi_{total}^n &= [2(C_{10}\lambda + C_{01})(\lambda^{-1} - \lambda^{-4})]^n + \sum_{i=1}^M \exp\left(-\frac{\Delta t}{\tau_i}\right) \Pi_{MW_i}^{n-1} + \\ &+ \frac{ak_i \tau_i}{\Delta t} \left[ 1 - \exp\left(-\frac{\Delta t}{\tau_i}\right) \right] \left[ (2(C_{10}\lambda + C_{01})(\lambda^{-1} - \lambda^{-4}))^n - (2(C_{10}\lambda + \right. \\ &\left. C_{01})(\lambda^{-1} - \lambda^{-4}))^{n-1} \right]\end{aligned}\quad (3.62)$$

which depends only on the hyperelastic and viscoelastic parameters, time increment and stretch increment.



## 4. FINITE ELEMENT SOLUTION

The purpose of this section is the comparison between the finite element prediction of the rubber like material behaviour with the solutions previously presented. Most of the finite element codes allows the modelling of hyper-viscoelasticity, such as the Abaqus (commercial) and the V-Biomech (academic). Since the closed-form solutions presented before are only valid for the uniaxial stress state, a case study comprising that stress state is proposed in order to evaluate the its accuracy.

### 4.1. Case study: uniaxial stress

The uniaxial compression test of a rubber like material is selected as case study. In order to describe the material behaviour, the Mooney-Rivlin constitutive model and long term viscous effects are considered. The Mooney-Rivlin constitutive model uses only 2 parameters, while the viscosity is given by two Maxwell elements. The parameters adopted for the hyper-viscoelastic model are presented on Table 4.1, and the time and displacement history indicated in the input file BIO are listed in

Table 4.2. Regarding the geometry of the deformable body, a unit cube is considered, as shown in Figure 4.1. Since the prescribed displacement on the top is 0.5 mm (see Table 4.2), the final stretch will be 0.5. The cube is discretized with 64 hexahedral finite elements using the GID software.

**Table 4.1.** Parameters of the Mooney-Rivlin constitutive model (hyperelasticity) and for the two Maxwell elements (viscoelasticity).

$C_{10}$	$C_{01}$	$ak_1$	$ak_2$	$\tau_1$	$\tau_2$
0.12	0.03	5.5	3.3	10	1

**Table 4.2.** Time and displacement history considered in the uniaxial compression test.

Step	1	2
Displacement [mm]	0	-0.5
Time [s]	0	6

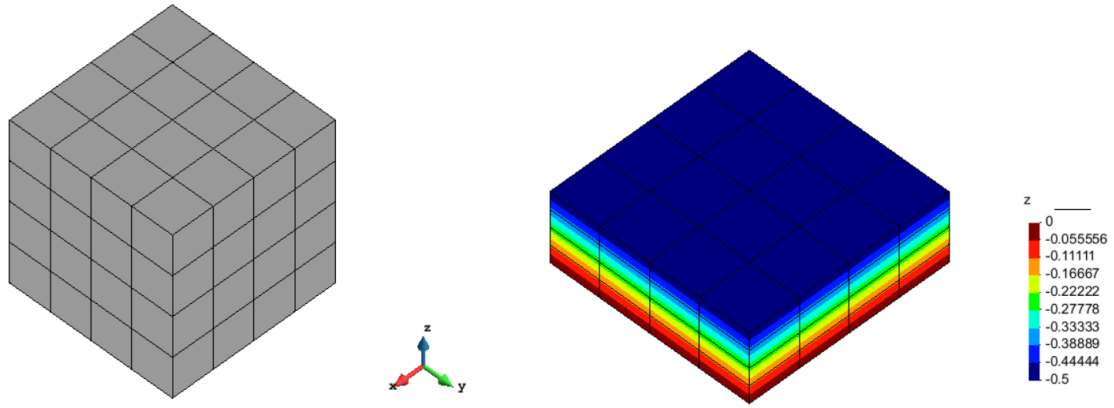


**Figure 4.1.** Discretization of the cube adopted in the numerical simulation of the uniaxial compression test and z displacement distribution after loading.

Regarding viscoelastic behaviour, the Prony series ( $\bar{g}_i^p$  and  $\tau_i$ ) are used in Abaqus to describe this behaviour, while the V-Biomech resorts to Maxwell element parameters ( $ak_i$  and  $\tau_i$ ). Prony series has the following formulation:

$$g_R(t) = G_0 \left( 1 - \sum_{i=1}^N \bar{g}_i^p \left( 1 - e^{\left( \frac{-t}{\tau_i} \right)} \right) \right) \quad (4.1)$$

where ( $\bar{g}_i^p$  and  $\tau_i$ ) are the parameters and  $N$  the number of Prony elements, which should be equal to the number of Maxwell elements. For  $t = 0 \rightarrow g_R(0) = G_0$  and for an infinite time  $g_R(\infty) = G_0(1 - \sum_{i=1}^N \bar{g}_i^p)$ . Revisiting equations (3.39) (3.40), which describe Maxwell elements formulation, the same conclusions must be made giving that for  $t = 0 \rightarrow \hat{\gamma}(0) = 1 + \sum_{i=1}^N ak_i$  and for an infinite time  $\hat{\gamma}(\infty) = 1$ . Matching the two expressions for the initial time we obtain:

$$G_0 = 1 + \sum_{i=1}^N ak_i \quad (4.2)$$

In order to obtain the Prony series parameters, both parcels of the relaxation function are multiplied by the following fraction:

$$\frac{1}{\mu_0 + \sum_{j=1}^N \mu_j}$$

After that, the following deduction attends to explain the achievement of those parameters:

$$\begin{aligned}
\hat{\Gamma}(t) &= \mu_0 + \sum_{i=1}^N \mu_i e^{\left(\frac{-t}{\tau_i}\right)} \Leftrightarrow \\
\Leftrightarrow \hat{\Gamma}(t) \left( \frac{1}{\mu_0 + \sum_{j=1}^N \mu_j} \right) &= \left( \mu_0 + \sum_{i=1}^N \mu_i e^{\left(\frac{-t}{\tau_i}\right)} \right) \left( \frac{1}{\mu_0 + \sum_{j=1}^N \mu_j} \right) \Leftrightarrow \\
\Leftrightarrow \frac{\hat{\Gamma}(t)}{\mu_0 + \sum_{j=1}^N \mu_j} &= \frac{\mu_0}{\mu_0 + \sum_{j=1}^N \mu_j} + \sum_{i=1}^N \frac{\mu_i}{\mu_0 + \sum_{j=1}^N \mu_j} e^{\left(\frac{-t}{\tau_i}\right)} \Leftrightarrow \\
\Leftrightarrow \frac{\hat{\gamma}(t) \mu_0}{\mu_0 + \sum_{j=1}^N \mu_j} &= 1 - \sum_{i=1}^N \frac{\mu_i}{\mu_0 + \sum_{j=1}^N \mu_j} + \sum_{i=1}^N \frac{\mu_i}{\mu_0 + \sum_{j=1}^N \mu_j} e^{\left(\frac{-t}{\tau_i}\right)} \Leftrightarrow \\
\Leftrightarrow \frac{\hat{\gamma}(t)}{\frac{\mu_0 + \sum_{j=1}^N \mu_j}{\mu_0}} &= 1 - \sum_{i=1}^N \bar{g}_i^p + \sum_{i=1}^N \bar{g}_i^p e^{\left(\frac{-t}{\tau_i}\right)} \Leftrightarrow \\
\Leftrightarrow \frac{\hat{\gamma}(t)}{1 + \sum_{i=1}^N ak_i} &= 1 - \sum_{i=1}^N \bar{g}_i^p \left( 1 - e^{\left(\frac{-t}{\tau_i}\right)} \right) \Leftrightarrow \\
\Leftrightarrow \hat{\gamma}(t) &= G_0 \left( 1 - \sum_{i=1}^N \bar{g}_i^p \left( 1 - e^{\left(\frac{-t}{\tau_i}\right)} \right) \right)
\end{aligned} \tag{4.3}$$

Thus, deducing that:

$$\bar{g}_i^p = \frac{\mu_i}{\mu_0 + \sum_{j=1}^N \mu_j} = \frac{ak_i}{1 + \sum_{j=1}^N ak_j} \tag{4.4}$$

For the given case study:

$$\begin{cases} \bar{g}_1^p = \frac{ak_1}{1 + ak_1 + ak_2} = \frac{5.5}{1 + 5.5 + 3.3} = 0.5612244898 \\ \bar{g}_2^p = \frac{ak_2}{1 + ak_1 + ak_2} = \frac{3.3}{1 + 5.5 + 3.3} = 0.3571428571 \end{cases}$$

Adopting the V-Biomech finite element code, the decomposition of the second Piola Kirchhoff stress into different components is presented in Figure 4.2 for the uniaxial compression test. The results are obtained using the material properties presented in Table 4.1 and assuming the mode I of viscoelasticity. The axial stress component is negative because the cube is under compression, but the evolution is non-linear. In this case, since  $ak_1 > ak_2$  and  $\tau_1 > \tau_2$ , the first Maxwell element has a larger impact in the solution in

comparison to the second one. On the other hand, the volumetric part of the hyperelasticity is higher than the deviatoric part, which contradicts equation (3.31) since it is only valid for the mode III of viscoelasticity.

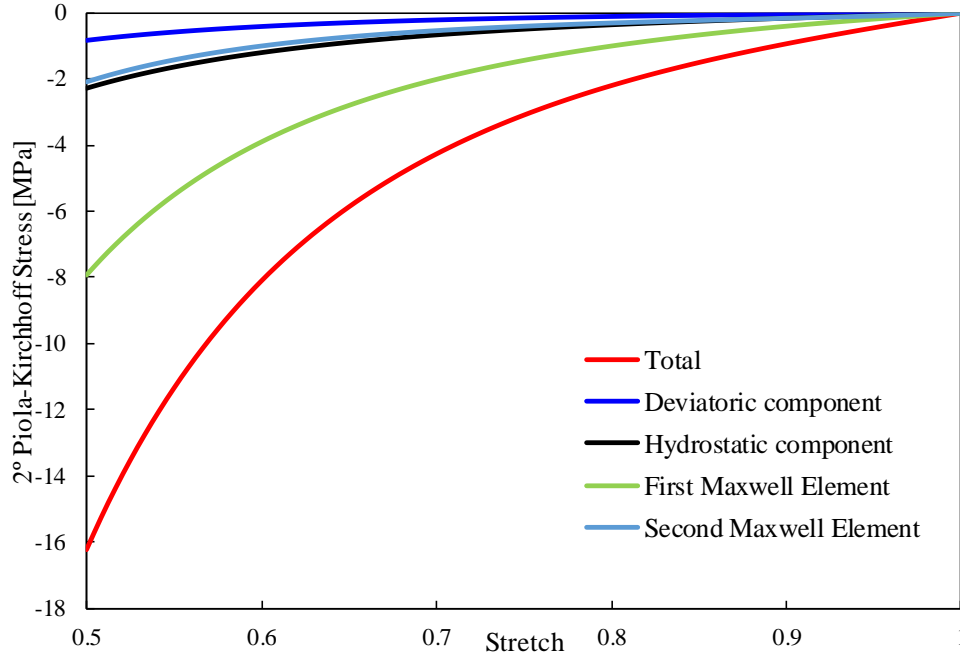


**Figure 4.2.** Contribution of each component composing the second Piola Kirchhoff stress in the uniaxial compression test.

## 4.2. Nearly incompressible behaviour

The formulation implemented in the V-Biomech finite element code only allows the modelling compressible and of nearly incompressible materials. By default, the bulk modulus, is given by:

$$K = 1000 \times 2(C_{10} + C_{01}) \quad (4.5)$$

while the shear modulus can be calculated by:

$$G = 2(C_{10} + C_{01}) \quad (4.6)$$

The Poisson ratio can be evaluated through the ratio between the bulk and the shear modulus by:

$$\nu = \frac{3K/G - 2}{6K/G + 2} \quad (4.7)$$

Table 4.3 presents the information about the Poisson ratio for some values of the ratio between bulk and the shear modulus. Since  $K/G = 1000$  is assigned by default in V-Biomech, the default Poisson ratio is 0.4995, which means nearly incompressible behaviour.

**Table 4.3.** Relationship between the ratio bulk /shear modulus and the Poisson ratio according to the V-Biomech finite element code.

$K/G$	Poisson ratio $\nu$
10	0.452
20	0.475
50	0.490
100	0.495
1000	0.4995
10000	0.49995

In order to fully characterize the hyperelastic behaviour in Abaqus, besides the constitutive model parameters,  $C_{10}$  and  $C_{01}$ , Abaqus also requests a parameter  $D$ , which reflects the material's Poisson ratio:

$$D = \frac{2}{K} \quad (4.8)$$

where  $K$  denotes bulk modulus. The incompressibility of the material is established when the parameter  $D$  is equal to zero. On the other hand, considering the material parameters presented in Table 4.1 and assuming nearly incompressible material definition (identical to the one adopted by default in V-Biomech), the parameter  $D$  should be:

$$D = \frac{2}{K} = \frac{2}{1000 \times 2(C_{10} + C_{01})} = \frac{2}{1000 \times 2(0.12 + 0.03)} = 0.006667$$

Although the material is assumed nearly incompressible in the finite element simulation, the closed-form solution obtained in the previous chapter for the hyperelastic behaviour (under uniaxial stress state) assumes that the material is incompressible. Neglecting the long viscous effects and considering the incompressible material behaviour, the second Piola-Kirchhoff stress in the loading direction defined by Mooney-Rivlin constitutive model is:

$$\Pi = 2(C_{10}\lambda + C_{01})(\lambda^{-1} - \lambda^{-4}) \quad (4.9)$$

The evolution of the second Piola Kirchhoff stress (axial component) in the uniaxial compression is presented in Figure 4.3, comparing the incompressible material behaviour (analytical) and nearly incompressible (V-Biomech simulation) assuming only hyperelastic behaviour (Mooney-Rivlin). Both solutions are almost coincident as highlighted

in Figure 4.3. The relative error is insignificant with an average value of 0.03%. Therefore, the presented closed-form solution for uniaxial compression of incompressible materials describes accurately the behaviour of nearly incompressible materials.

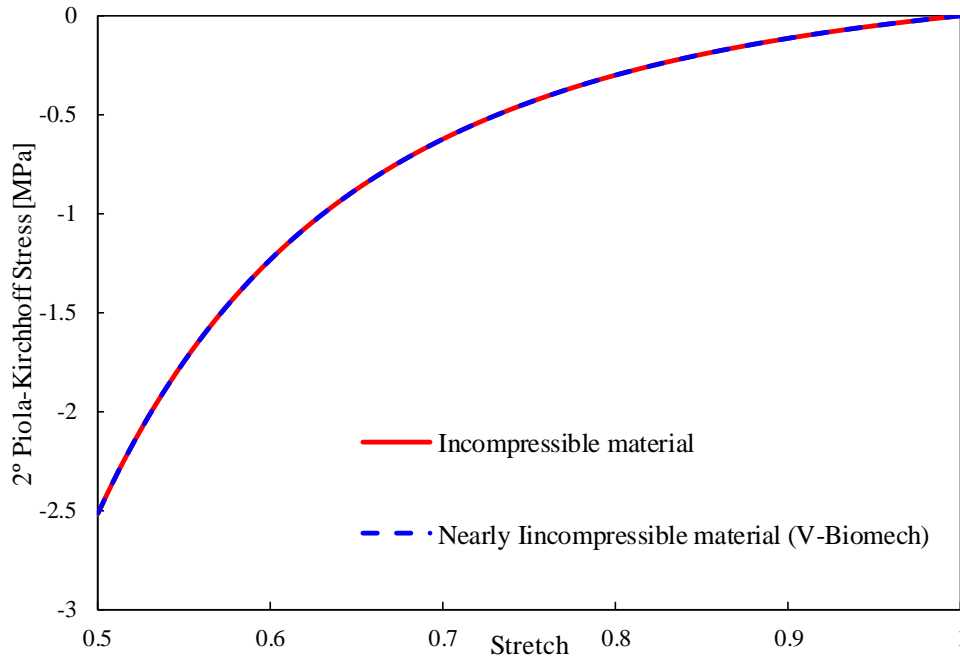


**Figure 4.3.** Comparison between incompressible material (analytical) and nearly incompressible (V-Biomech simulation) in the uniaxial compression test assuming only hyperelastic behaviour (Mooney-Rivlin).

### 4.3. Strain rate effect in viscoelasticity

Since large strains are commonly involved in the rubber materials, the strain rate is not constant in the uniaxial tensile test if the prescribed displacement is applied with constant velocity. Nevertheless, the velocity of the applied prescribed displacement dictates the nominal strain rate of the material, i.e. the strain rate at the beginning of the test. The influence of the prescribed velocity on the resulting second Piola-Kirchhoff stress in uniaxial tensile test is evaluated in this section. Since the total stress is defined by the generalized Maxwell model, both the upper and lower limits of the second Piola-Kirchhoff stress can be derived from equation (3.62). The minimum magnitude of the second Piola-Kirchhoff stress is obtained when the prescribed displacement is applied in an infinite time (zero velocity), i.e. the energy of the springs associated to the Maxwell elements is completely dissipated by the dashpots. Thus, the mechanical response is only characterized by the hyperelastic component of the stress:

$$\Pi_{\min} = \Pi_{\text{HE}} \quad (4.10)$$

On the other hand, the maximum magnitude of the second Piola-Kirchhoff stress is obtained when the prescribed displacement is applied instantaneously (infinite velocity), i.e. the dashpots associated to the Maxwell elements do not dissipated the energy of the springs. Therefore, the second Piola-Kirchhoff stress of the system is defined by the response of  $M+1$  springs in parallel, which can be described by:

$$\Pi_{\max} = \Pi_{\text{HE}} \left( 1 + \sum_{i=1}^M ak_i \right) \quad (4.11)$$

where  $M$  denotes the number of Maxwell elements. Taking into account equations (4.4) and (4.5), the maximum variation of the stress induced by the strain rate in the uniaxial compression test is directly proportional to the sum of  $ak_i$  of each Maxwell element.

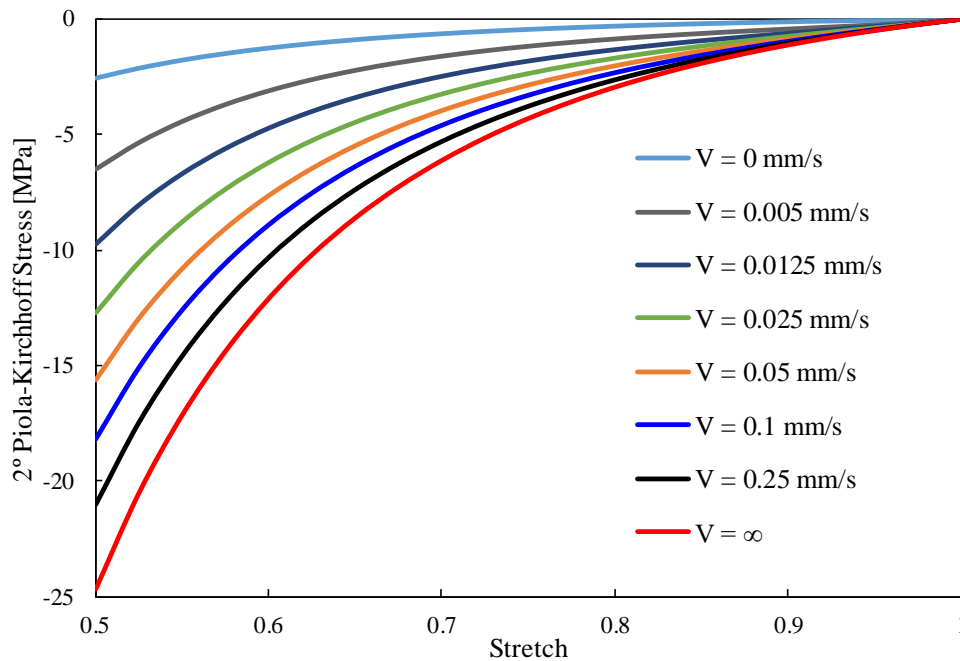


**Figure 4.4.** Influence of the prescribed displacement velocity on the predicted second Piola Kirchhoff stress considering the uniaxial compression test.

The V-Biomech was used to perform the numerical simulation of the uniaxial compression test in order to obtain the second Piola-Kirchhoff stress at different values of velocity on the surface with prescribed displacement. Figure 4.4 presents the evolution of the second Piola-Kirchhoff stress for eight values of prescribed displacement velocity, including the upper and lower limits previously defined. The stress magnitude increases

when the strain rate increases, as highlighted in Figure 4.4. Comparing the magnitude of the two stress limits, the stress value increases about 890% only by changing the value of the strain rate on the material.

#### **4.4. Viscoelasticity modes in V-Biomech**

The viscoelasticity modes currently implemented in V-Biomech finite element code are analysed and discussed in detail, in this section. The mode III of viscoelasticity takes in account both deviatoric and hydrostatic components of the hyperelasticity, while adopting the mode I only the deviatoric component plays a role. Therefore, since the contribution of each Maxwell element is dependent of the hyperelastic contribution, different solutions are expected in each mode. Figure 4.5 presents the decomposition of the second Piola Kirchhoff stress predicted in the uniaxial compression test into deviatoric and volumetric components, considering both the mode I and mode III of viscoelasticity. The deviatoric stress component from the hyperelastic behaviour is exactly the same in both modes, i.e. independent of the viscoelastic mode adopted. On the other hand, the volumetric stress component from the hyperelastic behaviour is largest in the mode I than in mode III. This results from the fact that the hydrostatic stress component in the mode III of viscoelasticity only balances the deviatoric stress component of the hyperelastic part, while considering the mode I the volumetric stress component must balance the total deviatoric stress (hyperelastic part and Maxwell elements). Therefore, adopting the mode III of viscoelasticity, the relationship between the deviatoric and volumetric stress components is always given by equation (3.31), independently of the Maxwell elements.



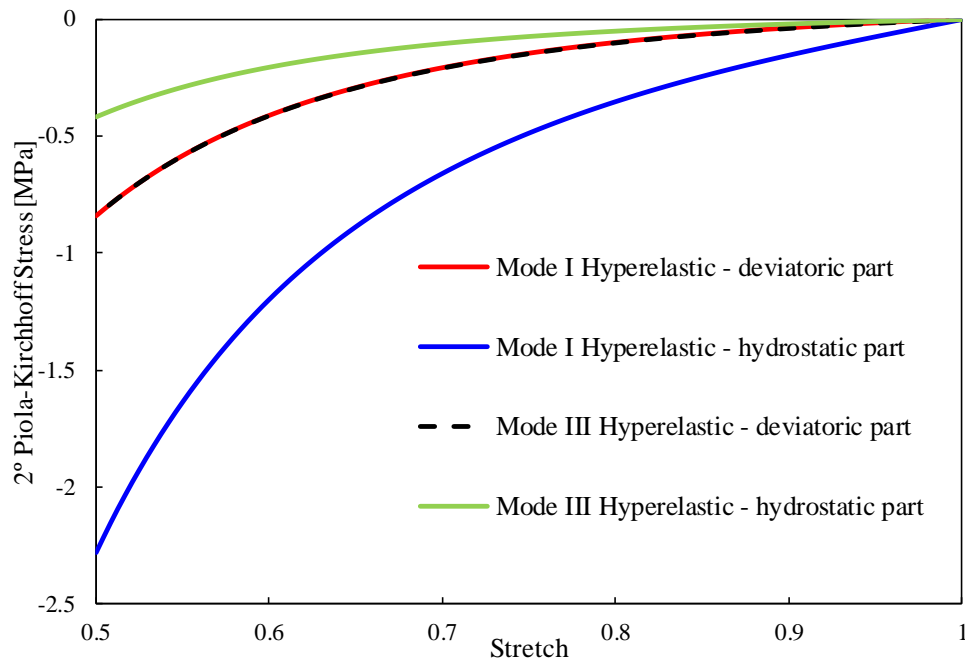


**Figure 4.5.** Deviatoric and volumetric stress components considering the mode I and mode III of viscoelasticity in the uniaxial compression test.

Since the ratio between the deviatoric and volumetric stress components is constant during the entire uniaxial compression test using the Mode III, the hydrostatic stress component can be easily evaluated from the total stress component through equation (3.31). Nevertheless, using the Mode I, the ratio between the deviatoric and volumetric stress components is unknown, and it is not constant during the uniaxial compression test. Accordingly, four different ways to predict the volumetric stress component were presented in section 3.3.2. Figure 4.6 shows the comparison between different predictions to approximate the hydrostatic stress component in the uniaxial compression test considering the mode I of the viscoelasticity. The prediction of the hydrostatic stress component given by equation (3.58) provides the most accurate solution, when compared with the solution obtained with the V-Biomech. However, the error increases with the stretch imposed in the unit cube, probably due to some loss of history that might be related to the second coefficient, which happens because the non-linearity of the stress evolution with the stretch.

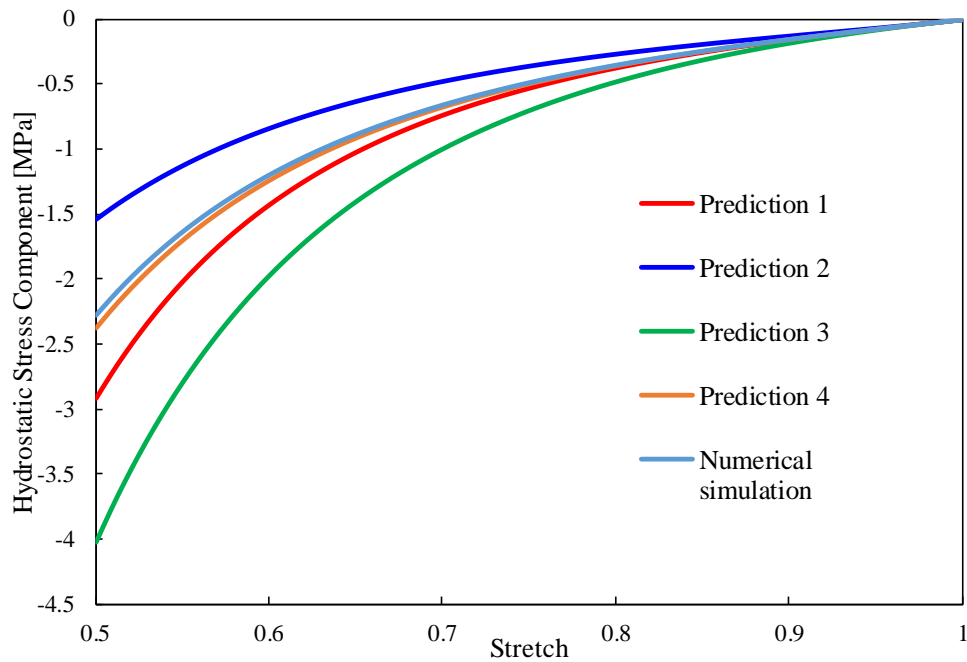


**Figure 4.6.** Comparison between different predictions for the hydrostatic stress component in the uniaxial compression test considering the mode I of the viscoelasticity.

## 4.5. Hyper-viscoelastic behaviour

The total stress (resulting from hyperelastic and viscoelastic) in the uniaxial compression test is evaluated considering both modes of viscoelasticity available in the V-Biomech finite element code, namely mode I and mode III described in section 3.3. The numerical solution is compared with the closed-form solution, derived in the previous chapter, in order to assess its accuracy. The solution is given by a recursive formula involving only the stretch value and the current time, see equation (3.61) and equation (3.62) for mode I and mode III, respectively.

Figure 4.7 presents the comparison of the second Piola Kirchhoff stress obtained by numerical simulation (V-Biomech) and predicted with equation (3.61) in case of mode I, and equation (3.62) in case of mode III. First of all, the numerical solution is different depending on the selected viscoelasticity mode (I or III). Although the mechanical behaviour is similar in both modes, the difference between them after loading (stretch of 0.5) is approximately 7% in the value of the second Piola Kirchhoff stress, as shown in Figure 4.7. Secondly, the solutions given by equations (3.61) and (3.62) are in good agreement with the finite element solutions. Indeed, the solution for the mode III presents an error inferior to 0.1%, while considering the mode I the maximum relative error is about 1.5%. Therefore,

the closed-form solutions for the second Piola Kirchhoff stress in the uniaxial stress are in very good agreement with the numerical solution, particularly in the case of mode III.

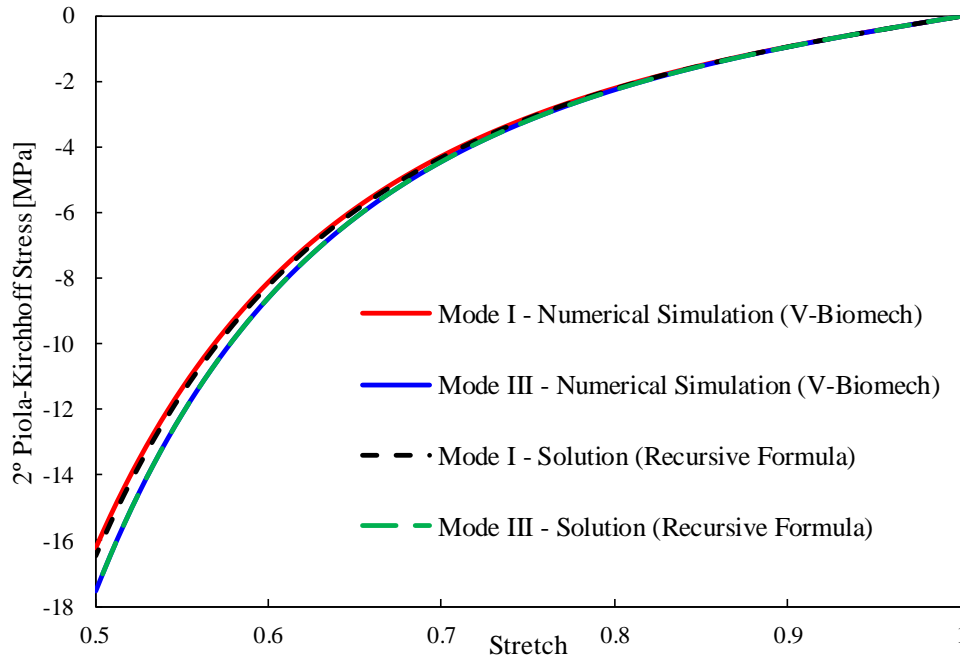


**Figure 4.7.** Comparison of the second Piola Kirchhoff stress obtained by numerical simulation (V-Biomech) and predicted with equation (3.61), in case of mode I and equation (3.62) in case of mode III.

## 4.6. Comparison between V-Biomech and Abaqus

Since the information about the viscoelasticity formulation implemented in Abaqus is not extensive and the source code is not available for the users, this section intends to compare numerical results obtained with Abaqus and V-Biomech.

The objective is to understand which viscoelasticity mode (I or III) is implemented in Abaqus. Therefore, the case study described in section 4.1 is simulated by both finite element codes under the same conditions. Nearly incompressible material is assumed in Abaqus software with  $D = 0,006667$ , as presented in equation (4.8). Although Abaqus allows the user to select several variables to be monitored during the simulation, the second Piola-Kirchhoff stress is not available. Thus, the component of the second Piola-Kirchhoff stress tensor in the loading direction (33) can be obtained from the Cauchy stress tensor assuming nearly incompressible behaviour by:

$$\Pi_{33} = \frac{\sigma_{33} J}{\lambda_3^2} \quad (4.12)$$

where  $J$  denotes the Jacobian, which is evaluated by the multiplication of the three stretches. In order to calculate the stretch in each direction, Abaqus allows the extraction of logarithmic strain components, which are converted into stretch by:

$$\lambda_3 = \exp(\text{LE}_{33}) \quad (4.13)$$

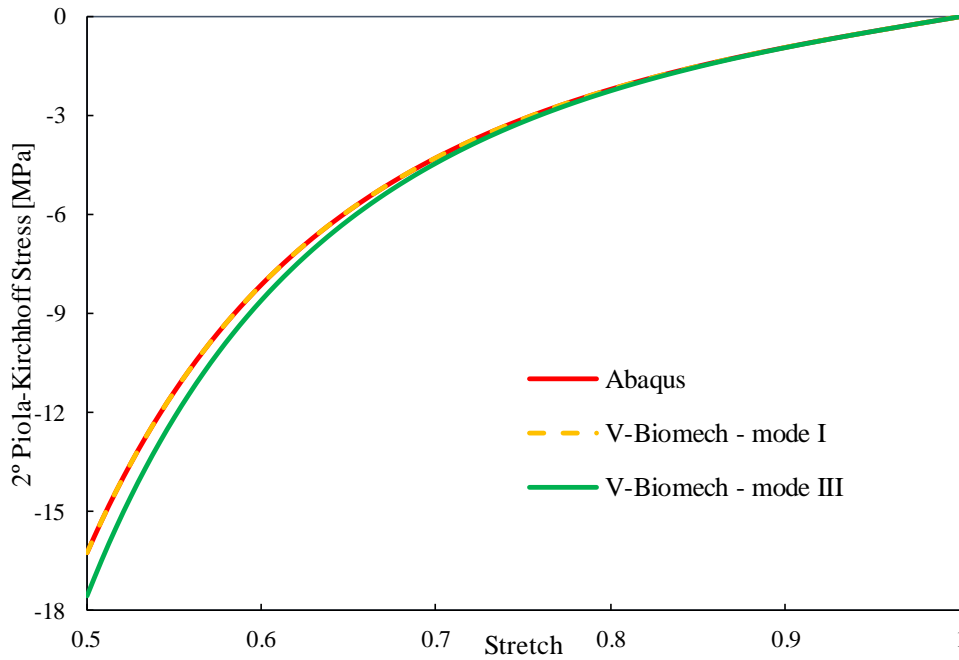


**Figure 4.8.** Comparison between the second Piola Kirchhoff stress predicted by Abaqus and V-Biomech (mode I and mode III) finite element codes in the uniaxial compression test.

Figure 4.8 shows the comparison between the Abaqus and V-Biomech results in terms of second Piola Kirchhoff stress in the uniaxial compression test. From the results, it is clear that the formulation implemented in Abaqus is similar to the one implemented in V-Biomech considering the mode I of viscoelasticity. Indeed, the difference between the second Piola Kirchhoff stress predicted by Abaqus and V-Biomech (mode I) is lower than 0.1%. Therefore, the comparison of results from Abaqus should only be done with results from V-Biomech using the mode I.

## 5. EXPERIMENTAL TESTS

This chapter presents the results of some experimental tests, namely the uniaxial compression of a cylindrical specimen and relaxation test for two different materials. The objective is to find the constitutive model parameters that characterize the available material and then replicate the experimental behaviour using V-Biomech and Abaqus software.

### 5.1. Experimental procedure and results

Two different polyurethane (PUR) sticks were acquired from “Norlene”, a Portuguese company that specializes in manufacturing and distributing technical plastics and rubber materials. Then, the polyurethane sticks (250 mm length and 18 mm of diameter for the orange PUR and 20 mm of diameter for the yellow PUR) were cut into cylindrical specimens with 18 mm of diameter and 25 mm of length, which are illustrated in Figure 5.1. The real dimensions and the hardness of both materials used in the experimental tests can be found in Table 5.1.

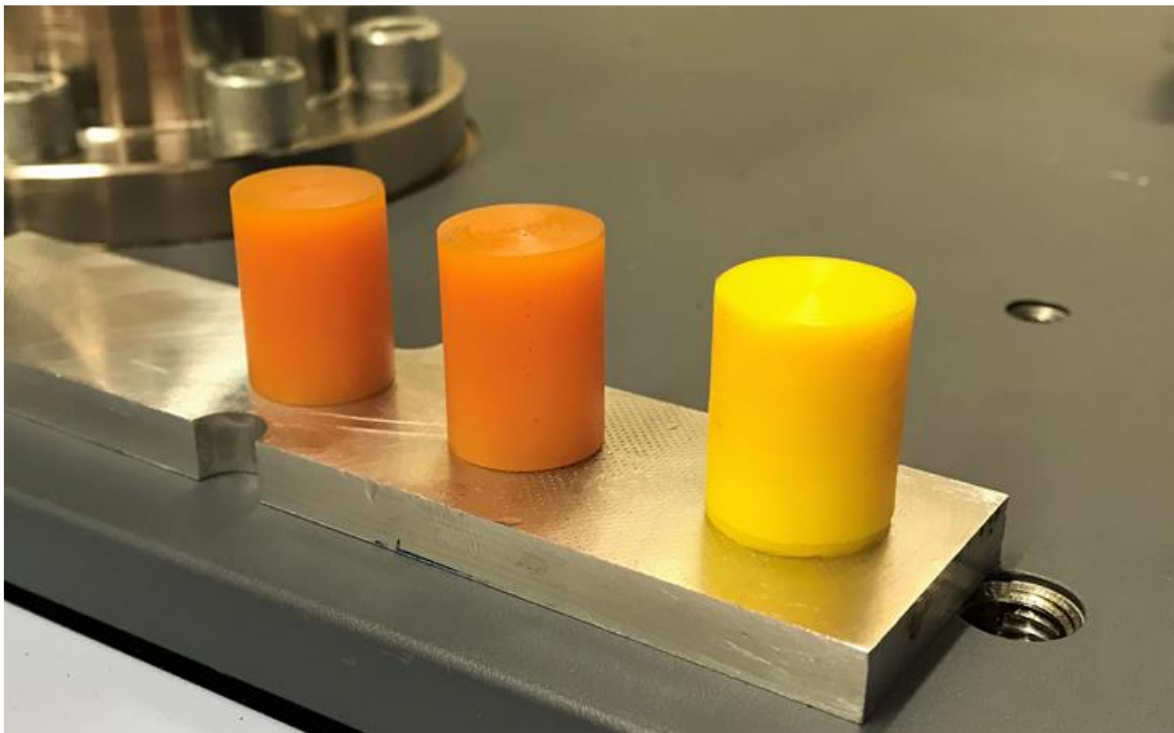


**Figure 5.1.** Test specimens after being properly cut to their desired shape and ready to use in the experimental tests.

**Table 5.1.** Dimensions (nominal and real) and hardness of both materials used in the experimental tests.

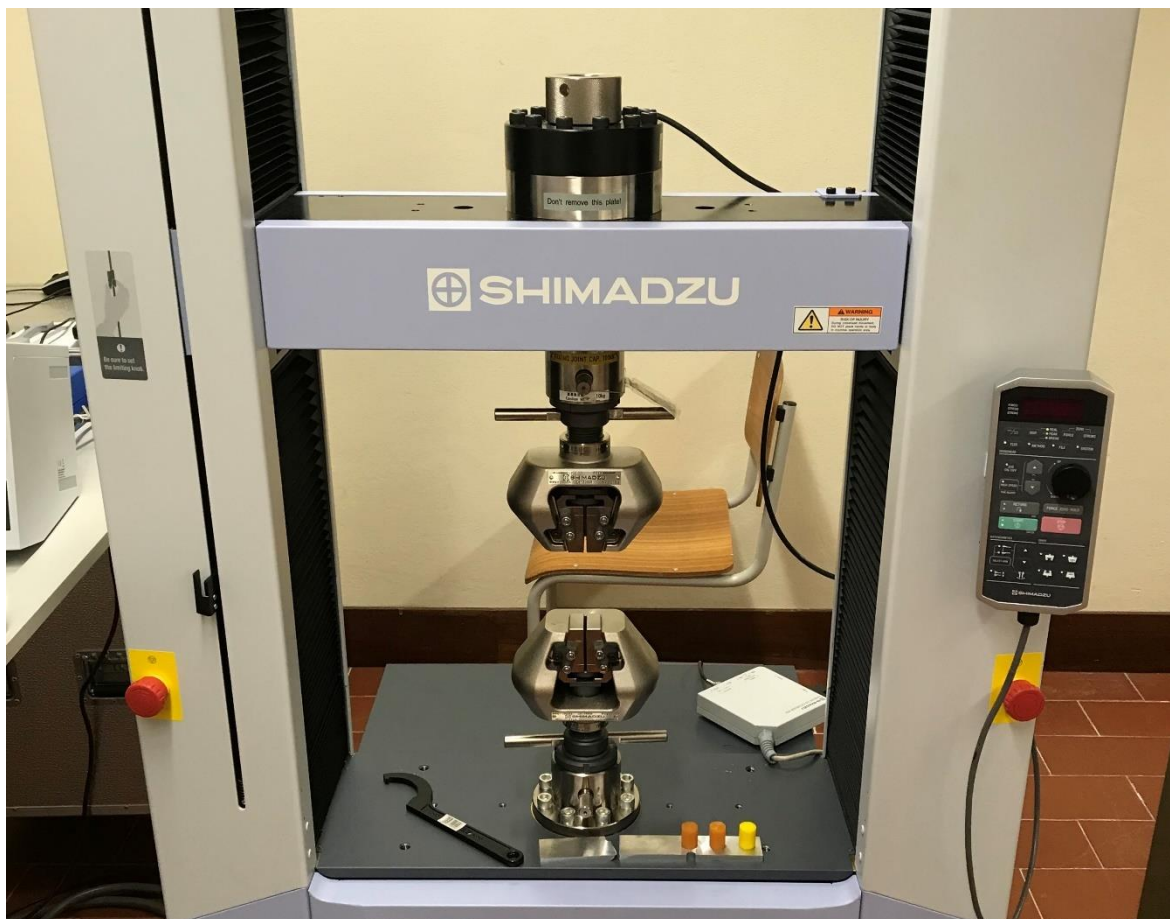
Test Specimens	Nominal Diameter [mm]	Real Diameter [mm]	Nominal Height [mm]	Real Height [mm]	Hardness [°Sh A]
Yellow	18	18.7	25	24.4	70
Orange	18	18.4	25	24.4	95

The accurate mechanical characterization of a given rubber material requires experimental data from different mechanical tests (tensile, compression, shear, biaxial, etc.). Thus, using only two types of test is not enough to have a good determination of the material parameters [18]. The Abaqus finite element code allows to model the mechanical behaviour directly from experimental data without given the material parameters of the constitutive model. However, it requires 4 different tests to evaluate the constants of the hyperelastic constitutive model: uniaxial test, volumetric test, planar shear test and biaxial test [19]. Since some of these tests might be difficult to carried out, in this dissertation the material parameters of the constitutive model are previously evaluated from only two tests, the uniaxial compression test and the relaxation test.

The work plan of the experimental tests can be found in Table 5.2. For each material (Yellow PUR and Orange PUR) three uniaxial compression tests and one relaxation test for will be performed. Notice that the uniaxial compression tests will be carried out at different values of grip velocity, while the relaxation test is obtained for the largest velocity in the compression phase. Furthermore, the prescribed displacement will be equal to all tests (8.75 mm), which gives a maximum stretch of 0.65. Figure 5.2 presents the Shimadzu tensile testing machine (maximum capacity of 100 kN) used in the experimental setup, whereas Figure 5.3 presents the lubrication (glycerine) used to diminish friction between the rubber and the improvised compression plates. Note that the extra orange PUR specimen is only there to act as a replacement in case of failure and therefore will not be tested.

**Table 5.2.** Experimental tests summary including test specimen, type of test, loading velocity and time.

Test number	Test specimen	Type of test	Loading velocity	Time
	-	-	mm/s	s
1	Yellow PUR	Compression test	5	1.75
2			0.5	17.5
3			0.05	175
4		Relaxation test	5	10000
5	Orange PUR	Compression test	5	1.75
6			0.5	17.5
7			0.05	175
8		Relaxation test	5	10000

**Figure 5.2.** Shimadzu tensile testing machine setup, combined with the yellow and orange PUR, and the improvised compression plates.



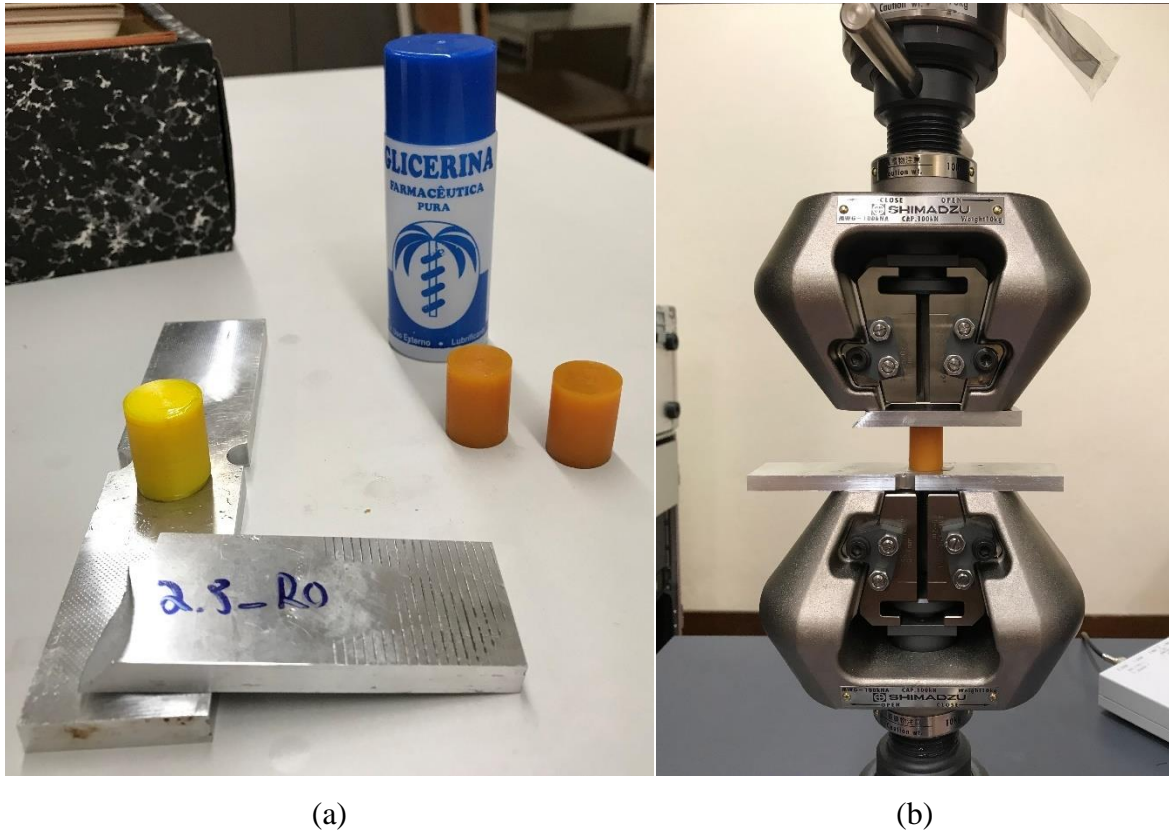


**Figure 5.3.** Experimental setup including: (a) the tests specimen, the lubrication used, the improvised compression plates and (b) the tensile testing machine.

During the experimental tests the tensile machine provides three variables: time  $t$ , force  $F$  and displacement  $\Delta l$ , which can be easily used to obtain the evolution of the second Piola-Kirchhoff stress  $\Pi$  and the stretch  $\lambda$ . Equation (4.12) provides the relation between the second Piola-Kirchhoff stress  $\Pi$  and Cauchy stress  $\sigma$ , which is equal to the force divided by the actual area of specimen where the force is imposed. Assuming incompressibility, the area can be calculated by the volume conservation theory:

$$A_i l_i = A_f l_f \quad (5.1)$$

which relates the initial area with the actual area. Assuming that the displacement is negative, since it is a compression test, the actual area is calculated by:

$$A_f = \frac{A_i l_i}{l_f} = \frac{A_i l_i}{l_i + \Delta l} \quad (5.2)$$

Furthermore, the stretch can be calculated with the following expression:

$$\lambda = \frac{l_f}{l_i} \quad (5.3)$$



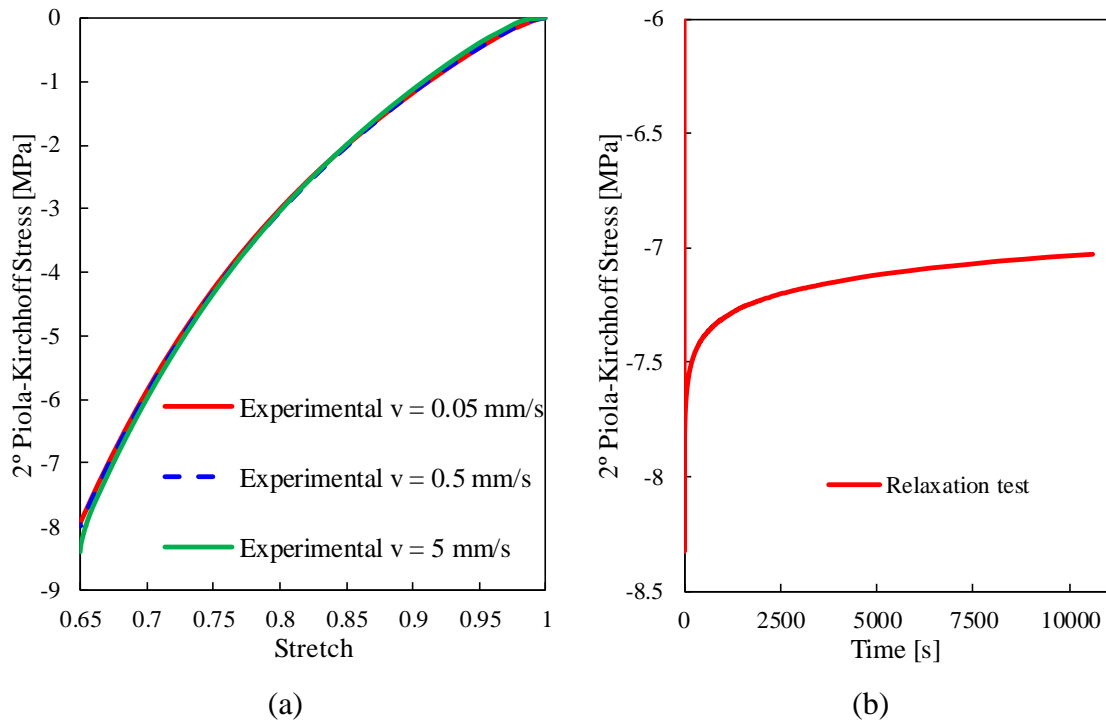


**Figure 5.4.** Experimental evolution of the second Piola Kirchhoff stress obtained from the yellow PUR experimental tests: (a) uniaxial compression tests at different values of grip velocity and (b) relaxation test.

Figure 5.4 shows the experimental results obtained for the yellow PUR (softest material). In Figure 5.4 (a), the evolution of the second Piola-Kirchhoff stress as a function of the stretch is evaluated for three different values of prescribed velocity, from where it can be concluded that this rubber material is not very sensitive to the loading velocity. Thus, leading to three nearly coincident stress-stretch curves. Note that the experimental test at the highest grip velocity seems to diverge from the other two tests while the stretch increases. After loading, the second Piola-Kirchhoff stress for the highest grip velocity is -8.4 MPa, whereas for other velocities is -8.0 MPa. Regarding the relaxation test (see Figure 5.4 (b)), the material seems to withstand a maximum second Piola-Kirchhoff stress of -8.3 MPa, throughout its loading phase, which is in line with the highest grip velocity compression test. Afterwards, the material experiences a relaxation phase of 10000 seconds (about 2.5 hours), which lead to a minimum second Piola-Kirchhoff stress of -7.0 MPa. Thus, allowing to conclude that the material relaxes 1.3 MPa in 10000 seconds.

Regarding the orange PUR (hardest material), Figure 5.5 (a) presents the evolution of the second Piola-Kirchhoff stress, as a function of the stretch, for three different values of prescribed velocity. These experimental compression tests prove that the loading behaviour is more complex, when compared to the softer yellow PUR material, with the

presence of an inflection point in each curve. Furthermore, Figure 5.5 (a) demonstrates that the orange PUR is much more sensible to the grip velocity, as shown through the distance between the three curves, but providing the same relative evolution. For the highest grip velocity, the orange PUR material presents a second Piola-Kirchhoff stress of -26.1 MPa for the final stretch of 0.65, whereas, for the slowest grip velocity, the material shows a second Piola-Kirchhoff stress of -23.7 MPa for the stretch value. As for the minimum second Piola-Kirchhoff stress in the relaxation, the orange PUR reaches a value of -18.0 MPa, therefore providing a relaxation of 6.4 MPa in 10000 seconds. Moreover, Figure 5.5 (b) shows that the relaxation stabilizes much quicker, when compared to the yellow PUR material (see Figure 5.4 (b)).

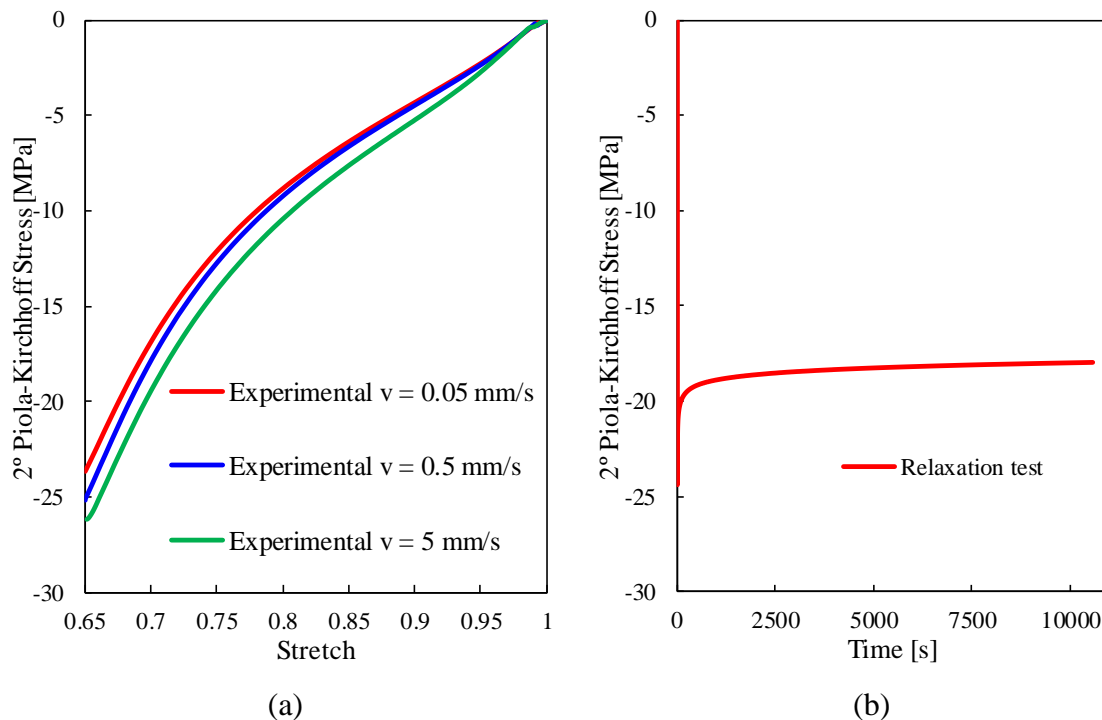


**Figure 5.5.** Experimental evolution of the second Piola Kirchhoff stress obtained from the orange PUR experimental tests: (a) uniaxial compression tests at different values of grip velocity and (b) relaxation test.

## 5.2. Material parameters identification – curve fitting

The experimental data previously presented is used in this section to calibrate the material parameters of the constitutive models adopted in the finite element simulation. The closed-form solutions for the uniaxial compression tests, obtained in chapter 3 for the mode I and III of viscoelasticity, are used in the identification of the material parameters. The main idea is the minimization of the difference between the experimental and the

numerical solution, using the stress-strain curves from the uniaxial compression test, as well as the relaxation test simultaneously. That procedure is carried out using the Microsoft Excel, specifically using the solver to obtain the set of material parameters that fits the experimental behaviour. Different options in terms of constitutive model are adopted in the present study in order to evaluate the accuracy of each one. Thus, regarding the hyperelasticity, the Mooney-Rivlin constitutive model is applied considering both 2 and 5 parameters. On the other hand, regarding the viscoelasticity, both 2 and 3 Maxwell elements are considered. Moreover, the curve fitting is performed for each material analysed and for the two different modes of viscoelasticity. Hence, four models are considered:

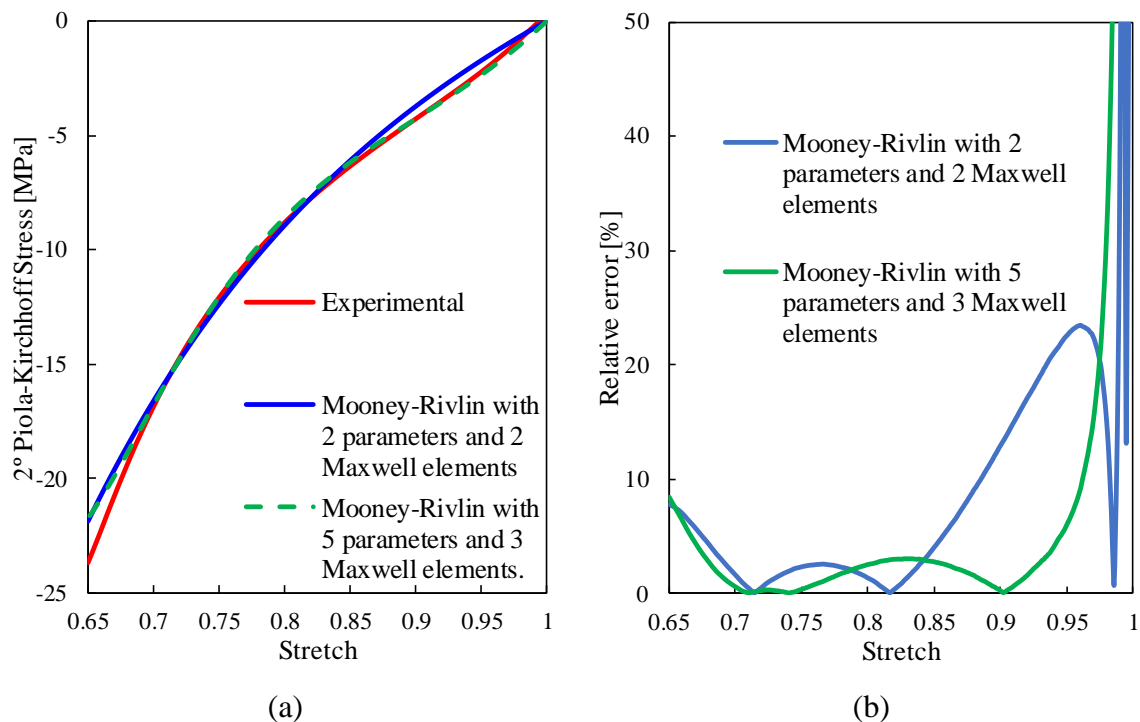
1. Mooney-Rivlin constitutive model with 2 parameters and 2 Maxwell elements.
2. Mooney-Rivlin constitutive model with 2 parameters and 3 Maxwell elements.
3. Mooney-Rivlin constitutive model with 5 parameters and 2 Maxwell elements.
4. Mooney-Rivlin constitutive model with 5 parameters and 3 Maxwell elements.

Although the flexibility of the constitutive model increases using more material parameters, allowing to describe more complex mechanical behaviour, the amount of experimental data required to perform a reliable identification of the material parameters increases also. Therefore, a balance between complexity of the constitutive model and the available experimental data is essential. The resulting set of parameters is presented in Table 5.3 for both materials (yellow PUR and orange PUR) and considering both viscoelasticity modes. The simplest model is adopted, i.e. the Mooney-Rivlin constitutive model with 2 parameters and 2 Maxwell elements.

Considering the yellow PUR, an accurate approximation of the mechanical behaviour is obtained using only 2 Mooney-Rivlin parameters and 2 Maxwell elements. On the other hand, the orange PUR presents an inflection point in the stress evolution during the uniaxial compression test, which was demonstrated in Figure 5.5 (a). Figure 5.6 (a) presents the comparison between the first and fourth combination methods for the orange PUR at the slowest velocity ( $v = 0,05 \text{ mm/s}$ ). The relative error evolution between the experimental data and the first and fourth combination methods is presented in Figure 5.6 (b). Since the improvement in the accuracy obtained using 5 parameters in the Mooney-Rivlin constitutive model and 3 Maxwell elements is not significant, the Mooney-Rivlin with 2 parameters and 2 Maxwell elements are adopted in order to simplify the numerical simulation. Notice that the other combinations were also analysed but did not retrieve any kind of advantage.

**Table 5.3.** Material parameters of the constitutive model (Mooney-Rivlin and Maxwell elements) identified for both materials and for both viscoelasticity modes.

	Yellow PUR	Yellow PUR	Orange PUR	Orange PUR
	Mode I	Mode III	Mode I	Mode III
$C_{10}$	1.67	1.67	5.55	5.56
$C_{01}$	-0.22	-0.22	-1.30	-1.30
$ak_1$	0.056	0.055	0.259	0.259
$ak_2$	0.094	0.093	1.136	0.997
$\tau_1$	3249	2897	142.1	134.6
$\tau_2$	143.2	132.5	0.125	0.126

**Figure 5.6.** Comparison between the experimental solution and the first and forth combination methods: (a) second Piola-Kirchhoff stress and (b) relative error.

### 5.3. Numerical model accuracy

The comparison between the experimental data and the results obtained by V-Biomech and Abaqus simulations is analysed for each material and both viscoelastic modes. The material parameters of the constitutive model (Mooney-Rivlin with 2 parameters and 2 Maxwell elements) listed in Table 5.3 are used in the finite element codes. Although the Abaqus have implemented only the mode I of viscoelasticity (see Figure 4.8), the set of

material parameters identified for the mode III is also used in the Abaqus for comparison purposes. The comparison between experimental and numerical evolution of the second Piola-Kirchhoff stress as a function of the stretch is presented in Figure 5.7 for both materials in the uniaxial compression test at 5 mm/s of velocity. Since the hardness of the yellow PUR is lower than the one of the orange PUR (see Table 5.1), the magnitude of the stress is lower in the yellow PUR for the same value of stretch. In fact, the stress in the orange PUR is about three times the value observed in the yellow PUR, as shown in Figure 5.7. The numerical results obtained with Abaqus and V-Biomech finite element codes are identical, while the effect of the viscoelasticity mode is not significant because different set of parameters are adopted for each mode (see Table 5.3). Although, all numerical solutions are in good agreement with the experimental ones, the modelling of the yellow PUR behaviour is more accurate than the orange PUR, which presents a more complex mechanical behaviour. Therefore, the modelling of the orange PUR can benefit from the adoption of more parameters in the Mooney-Rivlin constitutive model.

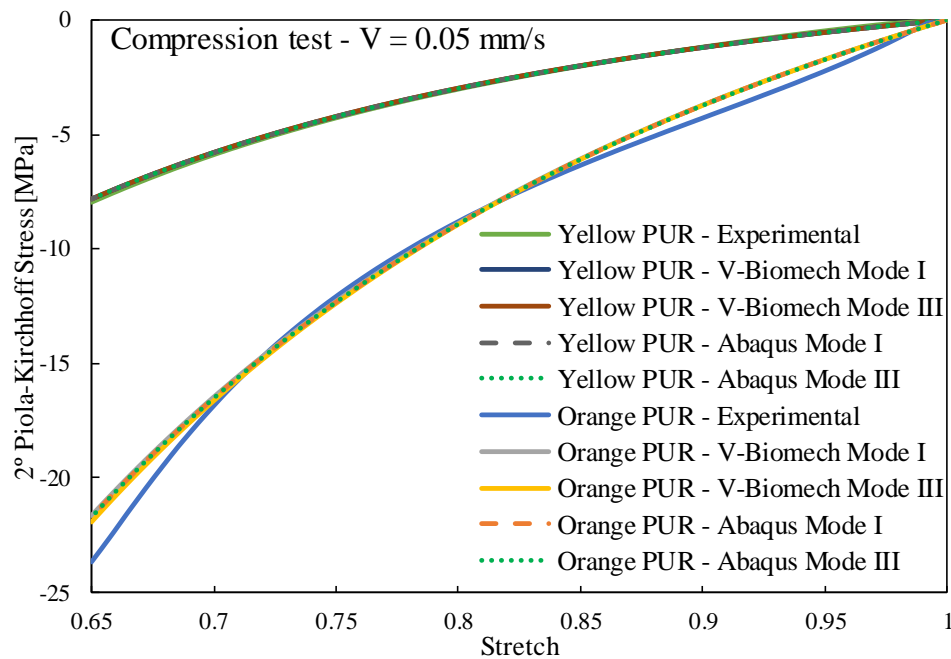


**Figure 5.7.** Stress-stretch comparison between the experimental results and the different solutions obtained for each material and viscoelasticity mode, while considering the slowest grip velocity of the compression tests.

**Table 5.4.** Last increment analysis for the experimental tests and the four simulations at different grip velocities, including the different materials and viscoelasticity modes.

		Second Piola-Kirchhoff stress $\Pi$ of the last increment				
	Loading Velocity	Experimental	V-Biomech Mode I	V-Biomech Mode III	Abaqus Mode I	Abaqus Mode III
	mm/s	MPa	MPa	MPa	MPa	MPa
ORANGE	5	-26.138	-25.535	-25.979	-25.545	-25.389
	0.5	-25.128	-23.549	-23.695	-23.558	-23.585
	0.05	-23.685	-21.697	-21.963	-21.704	-21.692
YELLOW	5	-8.427	-8.084	-8.07	-8.087	-8.072
	0.5	-7.988	-8.052	-8.042	-8.055	-8.038
	0.05	-7.947	-7.825	-7.836	-7.828	-7.802

Table 5.4 aims to highlight the difference between the simulation results, relating the second Piola-Kirchhoff stress in the final increment (stretch of 0.65). By analysing the last increment results, it is clear that Abaqus solution is much more related to V-Biomech mode I than the mode III. Moreover, it seems that the V-Biomech mode III might retrieve better results in approximating the experimental results. However, this results from the curve fitting, which is better adjusted to the experimental data.

Figure 5.8 presents the relaxation results comparison between the experimental tests and the simulations made for the different materials and different viscoelasticity modes. This analysis is coincident with the previous one, by demonstrating that the numerical solutions generate identical results. However, the accuracy of the finite element solution at the first 200 seconds of relaxation must be improved, particularly for the orange PUR. In fact, the stress relaxation is slower in the numerical solution than in the experimental measurements.

Since the Abaqus finite element code is adopted in the simulation of the rubber pad forming, the parameters that correspond to the mode I will be the used (see Table 5.3). Indeed, the formulation implemented in Abaqus is the one corresponding to mode I in V-bio, as shown in Figure 4.8.

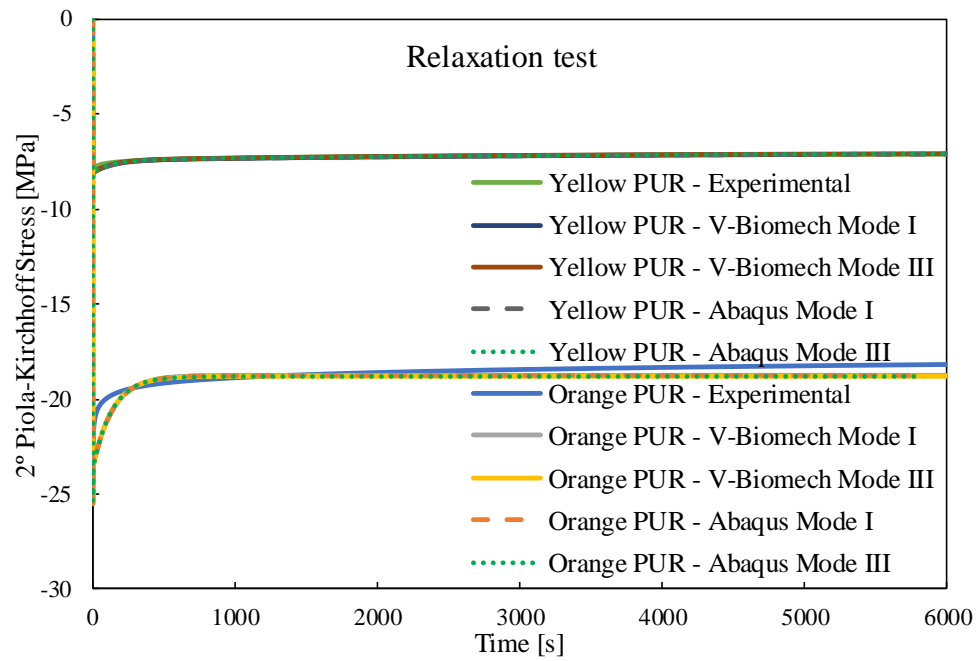


**Figure 5.8.** Stress-stretch comparison between the experimental results and the different solutions obtained for each material and viscoelasticity mode, while considering the relaxation tests.





## 6. RUBBER PAD FORMING SIMULATION

The application of the rubber pad forming in the production of metallic bipolar plates is analysed in this section. Focusing on the rubber pad forming of the bipolar plates, the desired geometry is obtained by plastic deformation induced by the three-way interaction between the sheet metal, the rubber punch and the die. Figure 6.1 presents the assembly of the three parts involved in the process and the contributions of each part. In this kind of forming process, there is no need for complex punch geometry since the die is the only tool that will shape the material. Therefore, the rubber pad that imposes the deformation in the sheet metal have a rectangular shape (cross section). Figure 6.2 shows the final geometry of the bipolar plate obtained by the conventional stamping.

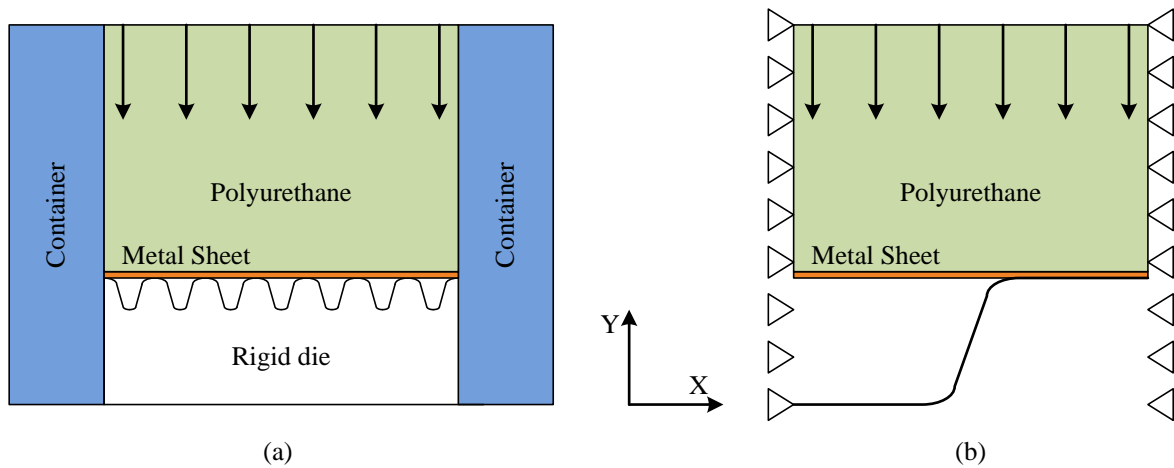


**Figure 6.1.** Rubber pad forming process assembly scheme: (a) original straight channel forming process and (b) the one used for finite element analysis.

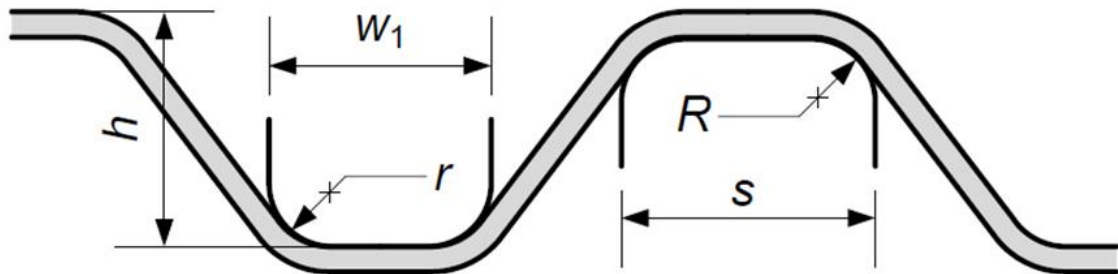


**Figure 6.2.** Sheet metal geometry in the conventional stamping for several channels.

The geometry of the bipolar plate and the sheet metal used by Neto et al [20] in the conventional stamping process, is adopted in this study. However, Abaqus software

(standard) is used to simulate the rubber pad forming process, using the same die geometry and sheet metal. Two different rubber materials are considered for the pad, which mechanical behaviour is defined by the parameters found in Section 5.

## 6.1. Finite element model

Serpentine flow design consists of two main areas: the straight and the U-bend channel sections indicated in Figure 6.3. In this study we will focus our efforts on analysing only the straight channel section. Due to symmetry conditions, only half-channel is simulated under plane strain conditions, therefore simplifying the model.

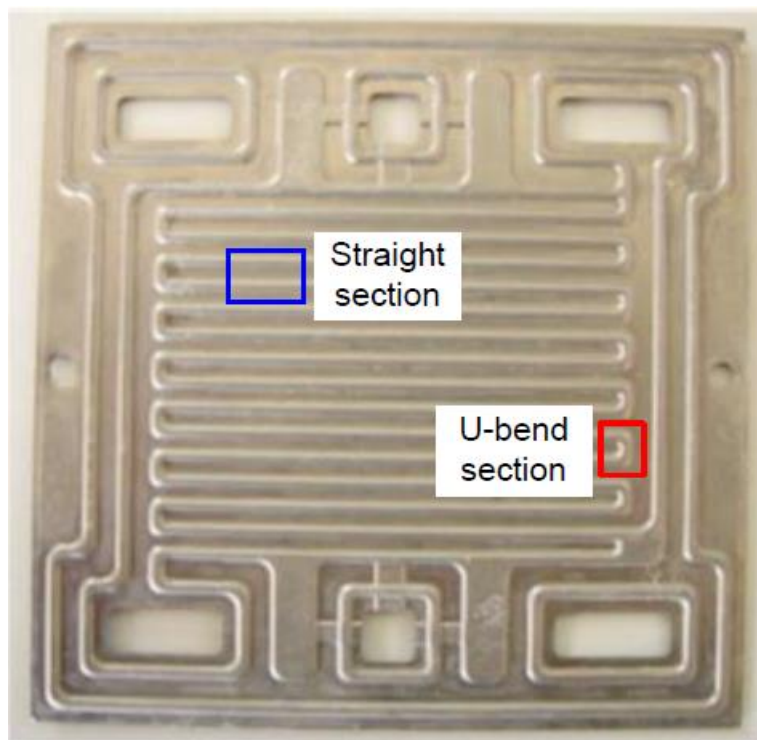


**Figure 6.3.** Example of a bipolar plate manufactured by forming.

**Table 6.1.** Reference values for the main dimensions of the desired product.

$w_1$	$s$	$h$	$r$	$R$
1.2 mm	1.2 mm	1.0 mm	0.3 mm	0.3 mm

The considered sheet metal is an austenitic stainless steel SS304 with thickness of 0.15 mm, which is commonly used in the sheet metal forming of bipolar plates. Considering the boundary conditions adopted in the simulation, the sheet length is 1.7 mm.

Its elastic behaviour is considered isotropic and constant, with a Young's modulus of 206.2 GPa and a Poisson ratio of 0.30. Its plastic response is described by Swift hardening law where the flow stress is given by:

$$Y = K(\varepsilon_0 + \bar{\varepsilon}^p)^n \quad \text{with} \quad \varepsilon_0 = \left(\frac{Y_0}{K}\right)^{1/n} \quad (6.1)$$

where  $\bar{\varepsilon}^p$  represents the equivalent plastic strain, while  $K$ ,  $\varepsilon_0$  and  $n$  are the material parameters, which can be found in Table 6.2. Regarding the mechanical behaviour of the rubber pad, nearly incompressible behaviour is assumed using  $D > 0$ , which can be found by equation (4.8). The simulations will be made using the parameters corresponding with the first viscoelasticity modes and can be found on Table 5.3..

**Table 6.2.** Material parameters used in the isotropic Swift hardening law to describe the metallic material.

$Y_0$ [MPa]	$K$ [MPa]	$n$
255.02	1481.84	0.508

Concerning the rubber pad process simulation, typically the die is assumed as rigid in numerical simulation, whereas the sheet metal is described by an elasto-plastic material model and the rubber punch by hyper-viscoelastic laws. Both the blank sheet and the rubber material are discretized with 2D linear finite elements (4 nodes), using a selective reduced integration technique in the sheet and hybrid integration (u/P formulation) for the rubber. Since the rubber pad is quite larger than the sheet metal, more elements are used in the zone in contact with the sheet metal because the Abaqus student edition only allows simulations with no more than 1000 nodes. Finally, the rubber pad has a height of 1.7 mm, which is yet another characteristic designed to keep the node count below the required by the student edition.

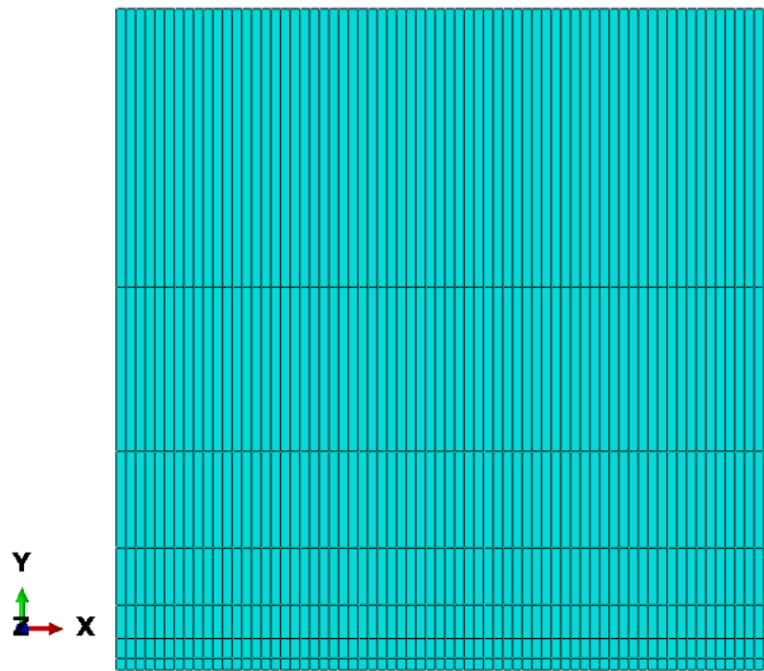


**Figure 6.4.** Rubber pad geometry and mesh used in the finite element analysis.

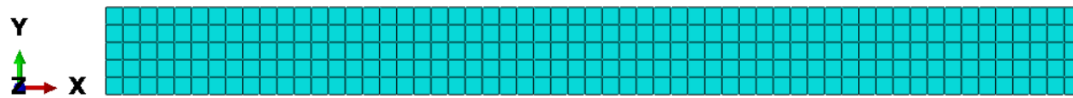


**Figure 6.5.** Sheet metal geometry and mesh used in the finite element analysis.

Figure 6.4 shows the Polyurethane rubber pad mesh, which is composed by 476 elements and 552 nodes and seven layers of elements with zone concentration in the contact area. Figure 6.5 presents the sheet metal mesh, which contains 285 finite elements and 348 nodes. Thus, our total assembly simulation presents 900 nodes. The contact conditions between parts are described by Coulomb's law, with a friction coefficient of 0.1. Due to symmetry conditions, the displacement of the nodes located in both extremities (left side and right side of the model) are constrained in the x-direction.

The numerical results from the rubber pad forming will be compared with the results from the conventional process simulation. Since both rubber materials characterized in Section 5 are used in the numerical simulation of the rubber pad forming, different values of prescribed displacement are required for each material due to the difference in the material hardness. Accordingly, in order to keep the loading velocity equal for both simulations, Table 6.3 defines the required time history and rubber displacement to accomplish full contact, while avoid further unnecessary compression. Note that desired bipolar plate

geometry is achieved for 0.8 mm of displacement for the yellow PUR, while for the orange PUR the desired geometry is achieved for 0.62 mm of prescribed displacement.

**Table 6.3.** Loading velocity, time history and rubber displacement for both rubber materials.

Test Specimens	Loading velocity [mm/s]	Time history [s]	Rubber displacement [mm]
Yellow PUR	0.2	5	1.0
Orange PUR	0.2	3.5	0.7

## 6.2. Results and discussion

The numerical results of the rubber pad forming obtained with the Abaqus finite element code are compared with the ones from the conventional stamping presented in [20]. Hence, the main results analysed are: the final thickness distribution, maximum thinning, the punch force and equivalent plastic strain.

Figure 6.6 presents the predicted von Mises stress distribution in the sheet and rubber at four different instants of the rubber pad forming considering the orange PUR rubber. The same figure presents three important points: (1) refers to the upper corner, where is expected to occur maximum thinning; (2) attends to the lower corner and (3) to the contact point on the left. Moreover, the stress imposed in the metal sheet is much higher than the rubber pad stress, and it reaches its maximum in the upper corner, i.e. point (1). The fillet radius of the flow channel is the last portion of the geometry to be shaped.

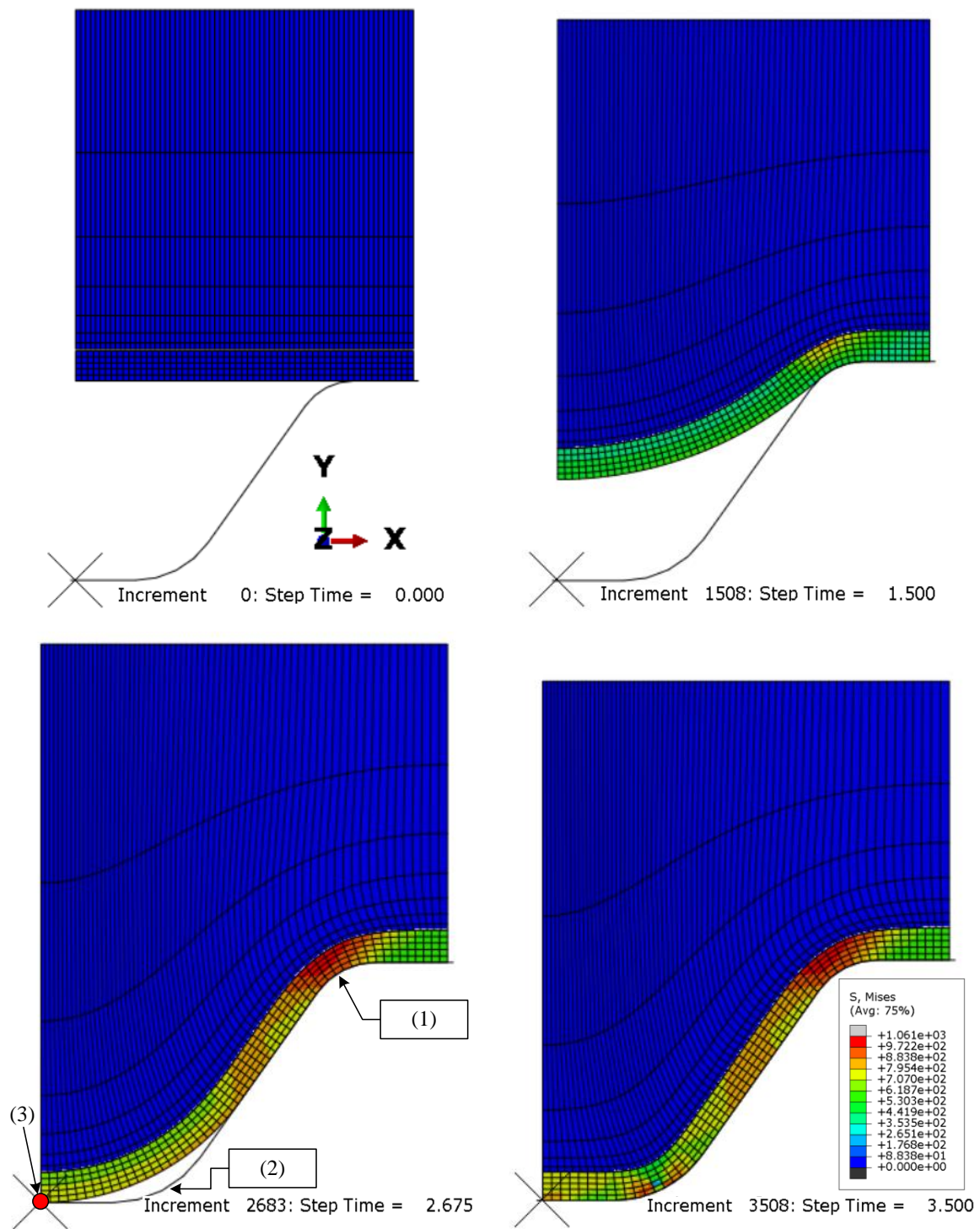


**Figure 6.6.** Predicted von Mises stress distribution in the sheet and rubber at four different instants of the rubber pad forming considering the orange PUR in the rubber.

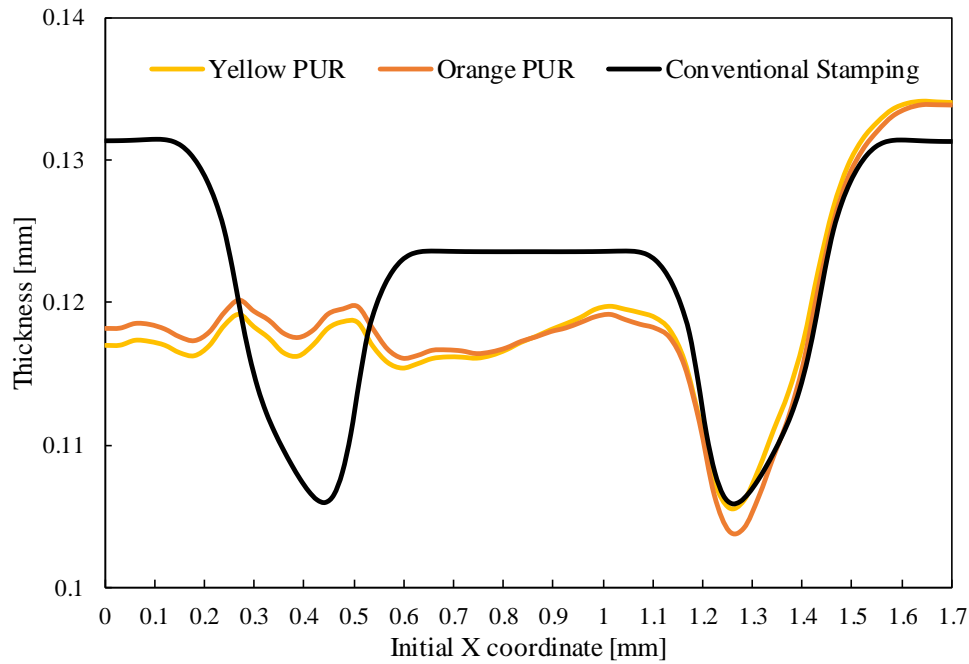


**Figure 6.7.** Comparison of final thickness distribution as function of the initial x coordinate, considering two different rubbers in the rubber pad forming and the conventional stamping process.

Figure 6.7 shows the final thickness distribution as a function of the initial x coordinate, comparing the results of the rubber pad forming (considering two different materials for the rubber) with the results from the stamping process. Considering the rubber pad forming, the largest thickness reduction occurs near point (1). Moreover, from the three simulations, the orange PUR material is the one that enforces larger thickness reduction in point (1), with the yellow PUR showing thickness results similar to the conventional stamping process. Since the orange PUR presents higher stiffness in comparison with the yellow PUR, the required force applied is also higher (see Figure 6.8). Therefore, for the same value of friction coefficient in both PUR materials, the friction forces are higher in orange PUR, which restrains the sliding between rubber and sheet, as well between sheet and rigid die. This can be the reason why the final thickness in the curvature (1) is lower adopting the orange PUR, while in curvature (2) the final thickness is higher using the orange PUR, as shown in Figure 6.7. Finally, the rubber pad forming provides less overall thickness reduction, when compared to the classic stamping process. Indeed, the thickness near the curvature (2) is significantly improved using the rubber forming simulation, for both rubber materials.

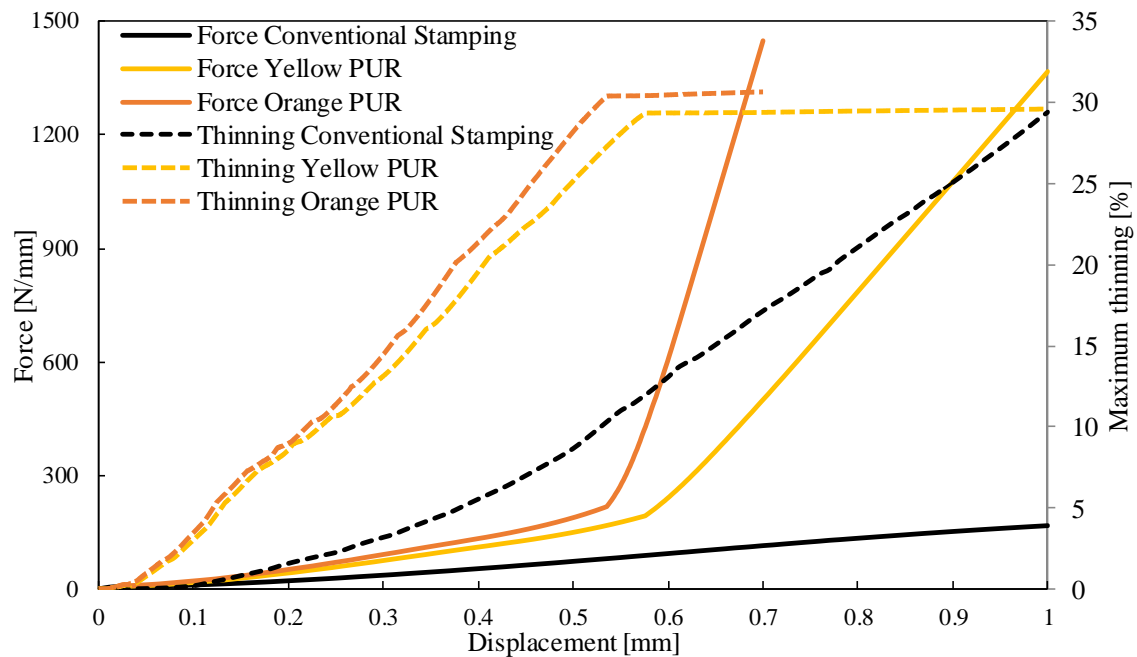


**Figure 6.8.** Evolution of the maximum thinning and punch force for both rubber material in the rubber pad forming of a bipolar plate and comparison with the conventional stamping.

Figure 6.8 shows the evolution of the predicted maximum thinning and force applied as a function of the displacement. Note that the indicated displacement refers to the prescribed displacement on the rubber upper surface, while in the conventional stamping simulation refers to the punch displacement. Thus, we cannot directly relate the displacement of the rubber with the punch, which does not allow a direct comparison between the variable in axis Y. The required forming force is higher in the rubber pad forming since the force required to deform the metal sheet is joined by the extra force required to compress the rubber material. Looking back, the use of such a small rubber pad (height of 1.7 mm) might have not been an adequate choice because the small pad height requires more deformation (compression) to achieve the desired geometry of the bipolar plate. Therefore, in the rubber pad forming the predicted force presents a sudden increase, which occurs when the sheet metal begins contact with the rigid die at point (3). Moreover, there is a clear correlation between the force and maximum thinning evolutions, i.e., when a sudden increase of the force is generated, the maximum thinning stabilizes. From this analysis one could extrapolate that, if an infinite large rubber pad was used, the force applied in the rubber pad simulation would converge to the force applied in the conventional stamping process.



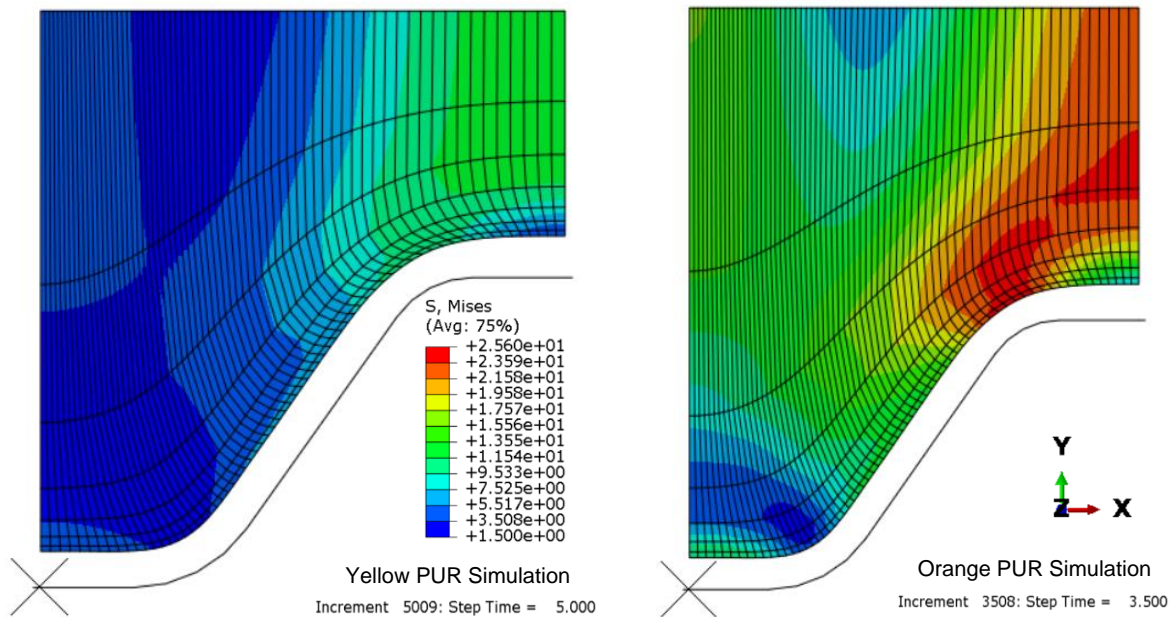


**Figure 6.9.** Predicted von Mises stress distribution in the rubber at the end of the forming process comparing two different materials for the rubber.

Figure 6.9 shows the comparison between the orange and yellow PUR in terms of Cauchy stress distribution after forming. As expected, the orange PUR presents the higher stress values when compared to the softer yellow PUR. The maximum second Piola-Kirchhoff stress value attained in the experimental uniaxial compression tests (chapter 5) are listed in Table 5.4, which is for the yellow PUR 8.427 MPa, and for the orange PUR is 26.138 MPa. These stress values can be easily converted to Cauchy stress, resulting in a maximum stress of 3.56 MPa for the yellow PUR and 11.08 MPa for the orange PUR. Comparing these experimental values with the maximum stress values predicted by simulation, the stress is much higher in some rubber zones. Thus, the level of compression is higher in the simulation process, which indicates that the experimental material characterization might not be totally corrected. On the other hand, increasing the pad height leads to a reduction of the strain in the rubber.

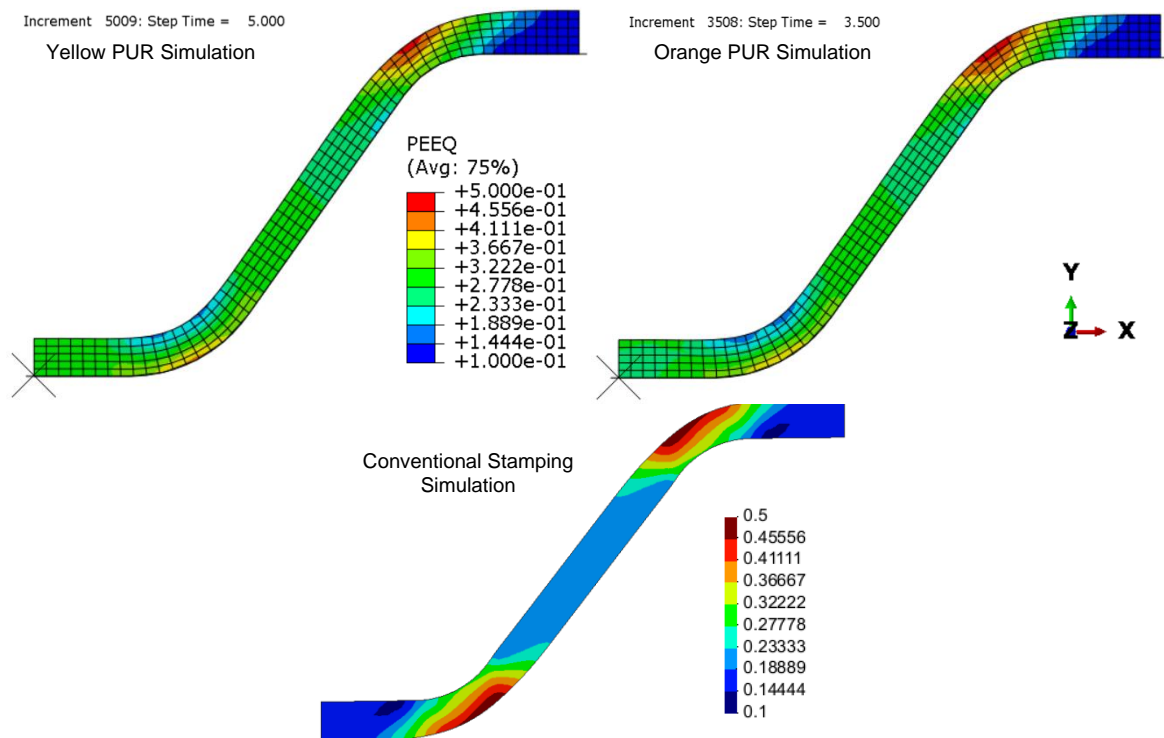


**Figure 6.10.** Equivalent plastic strain distribution on both rubber pad process simulation and the conventional stamping process.

Figure 6.10 presents the equivalent plastic strain distribution of the sheet at the end of forming, comparing the rubber pad forming with the conventional stamping process. The predicted equivalent plastic strain is related with the final thickness distribution (Figure 6.7), i.e. small plastic deformation leads to small thickness reduction. Regarding the point (3), the plastic deformation in the conventional stamping process is clearly smaller than in comparison with the rubber pad processes, which is in agreement with the higher thickness. On the other hand, the plastic deformation in the curvature zone (2) is higher in the conventional stamping, which justifies the thickness difference both forming processes. Finally, both the plastic deformation and the final thickness are similar in the curvature (1).

## 7. CONCLUSIONS

In the last years, the fuel cells emerged as one promising candidate to replace internal combustion engines in the automotive industry. The key components of a proton exchange membrane fuel cell are the bipolar plates, which can be manufactured by forming processes. This study presents a comprehensive analysis of the rubber pad forming process, which is a promising technology to replace the conventional stamping of metallic bipolar plates. Accordingly, the mechanical behaviour of the rubber pad involved in this forming process is a key point in the finite element simulation. Hence the hyper-viscoelastic behaviour of the rubber like materials is presented in detail, where the hyperelastic behaviour is described by the Mooney-Rivlin model, while the viscoelasticity is modelled by series of Maxwell elements.

Considering the uniaxial stress state, the closed-form solutions are derived for the mechanical modelling of synthetic rubbers. Since two different viscoelasticity modes are currently implemented in the V-Biomech finite element code, the closed-form solution is presented for each one. In mode I, the stress associated to the Maxwell elements is derived only from the deviatoric component of hyperelasticity, while mode III takes into account the total hyperelastic stress (deviatoric and hydrostatic contributions). Regarding the mode III, the proposed closed-form is in total agreement with the finite element solution, while the predicted hydrostatic stress, in the mode I, is slightly overestimated. However, mode III seems to establish a more reasonable way to include the viscoelasticity component.

In order identify the material parameters of the constitutive model, both the uniaxial compression of a cylindrical specimen and the relaxation test were carried out for two different materials (polyurethanes). From experimental data, the studied rubber materials are not very sensitive to the loading velocity, particularly the yellow PUR. Moreover, the stress level in the uniaxial compression test obtained for the orange PUR is about three times higher when compared with the yellow PUR. For both rubber materials analysed, the predicted behaviour is in good agreement with the experimental values, specifically the stress-strain curves from the uniaxial compression test and the relaxation test. Nevertheless, the experimental behaviour of the orange PUR is more complex than the

one of the yellow PUR, requiring more advanced constitutive models to achieve the same level of accuracy.

The production of bipolar plates by means of the rubber pad forming process is numerically analysed using plane strain conditions. The results are compared with the ones obtained from the conventional stamping process. This innovative process allows for a more uniform final thickness distribution, when compared to the classic stamping method. Nevertheless, the maximum thinning at the end is approximately the same in both forming processes. On the other hand, the forming forces are significantly higher in the rubber pad forming, presenting a sudden increase when the sheet contacts the rigid die in the channel bottom. Furthermore, the numerical results of the rubber pad forming process show that the final thickness of the stamped bipolar plate is not significantly influenced by the rubber hardness. Moreover, the maximum value of thinning occurs always in the fillet radius of the rib, which is the zone with large plastic deformation.

Finally, the proposed future objectives regarding the rubber forming project are: expand the experimental characterization of the available rubbers to fully characterize its mechanical behaviour, numerical simulation of the rubber pad forming using the full model of the bipolar plates and develop an experimental prototype of the setup.

## BIBLIOGRAPHY

- [1] Y. Liu and L. Hua, “Fabrication of metallic bipolar plate for proton exchange membrane fuel cells by rubber pad forming,” *J. Power Sources*, vol. 195, no. 11, pp. 3529–3535, 2010.
- [2] R. Taherian, “A review of composite and metallic bipolar plates in proton exchange membrane fuel cell: Materials, fabrication, and material selection,” *J. Power Sources*, vol. 265, pp. 370–390, 2014.
- [3] J. Wang, “Theory and practice of flow field designs for fuel cell scaling-up: A critical review,” *Appl. Energy*, vol. 157, 2015.
- [4] S. K. De and J. R. White, *Rubber Technologist’s Handbook*, no. vol. 1. Rapra Technology Limited, 2001.
- [5] W. N. Findley, J. S. Lai, and K. Onaran, *Creep and Relaxation of Nonlinear Viscoelastic Materials: With an Introduction to Linear Viscoelasticity*. Dover, 1976.
- [6] J. L. Alves, N. Yamamura, T. Oda, and C. Teodosiu, “Numerical simulation of musculo-skeletal systems by V-Biomech,” 2010.
- [7] O. C. Zienkiewicz, R. L. Taylor, J. Z. Zhu, O. C. Zienkiewicz, R. L. Taylor, and J. Z. Zhu, “Chapter 1 – The Standard Discrete System and Origins of the Finite Element Method,” in *The Finite Element Method: its Basis and Fundamentals*, 2013, pp. 1–20.
- [8] L. E. Malvern, *Introduction to the mechanics of a continuous medium*. Prentice-Hall, 1969.
- [9] J. L. Alves, “Simulação numérica do processo de estampagem de chapas metálicas,” Universidade do Minho, 2003.
- [10] M. Kaliske, L. Nasdala, and H. Rothert, “On damage modelling for elastic and viscoelastic materials at large strain,” *Comput. Struct.*, vol. 79, no. 22–25, pp. 2133–2141, Sep. 2001.
- [11] A. Castro, “Development of a biomimetic finite element model of the intervertebral disc diseases and regeneration,” *PQDT - Glob.*, p. 235, 2013.
- [12] P. A. L. S. Martins, R. M. N. Jorge, and A. J. M. Ferreira, “A Comparative Study of Several Material Models for Prediction of Hyperelastic Properties: Application to

- Silicone-Rubber and Soft Tissues,” *Strain*, vol. 42, no. 3, pp. 135–147.
- [13] M. Wadham-Gagnon, *Hyperelastic Modelling of Rubber Behaviour in Finite Element Software*, no. August. 2007.
- [14] O. H. Yeoh, “Characterization of elastic properties of carbon-black-filled rubber vulcanizates,” *Rubber Chem. Technol.* 63, 1990.
- [15] N. Kumar and V. V. Rao, “Hyperelastic Mooney-Rivlin Model : Determination and Physical Interpretation of Material Constants,” *MIT Int. J. Mech. Eng.*, vol. 6, no. 1, pp. 43–46, 2016.
- [16] A. Kossa, “Closed-form stress solutions for incompressible visco-hyperelastic solids in uniaxial extension,” *ZAMM - J. Appl. Math. Mech. / Zeitschrift für Angew. Math. und Mech.*, vol. 97, no. 10, pp. 1268–1282.
- [17] M. Kaliske and H. Rothert, “Formulation and implementation of three-dimensional viscoelasticity at small and finite strains,” *Comput. Mech.*, vol. 19, no. 3, pp. 228–239, 1997.
- [18] K. M. O. Hsiao and F. Y. Hou, “Nonlinear finite element analysis of elastic frames,” *Comput. Struct.*, vol. 26, no. 4, pp. 693–701, 1987.
- [19] M. Shahzad, A. Kamran, M. Z. Siddiqui, and M. Farhan, “Mechanical Characterization and FE Modelling of a Hyperelastic Material,” *Mater. Res.*, vol. 18, no. 5, pp. 918–924, 2015.
- [20] D. M. Neto, M. C. Oliveira, N. Marques, J. L. Alves, and L. F. Menezes, “Numerical study on the formability of metallic bipolar plates for proton exchange membrane fuel cells,” 2017.